Microgravity Change During the 2008–2018 Kīlauea Summit Eruption
Nearly a Decade of Subsurface Mass Accumulation

Koymans, M. R.; de Zeeuw-van Dalfsen, E.; Evers, L. G.; Poland, M. P.

DOI
10.1029/2022JB024739

Publication date
2022

Document Version
Final published version

Published in
Journal of Geophysical Research: Solid Earth

Citation (APA)
Koymans, M. R., de Zeeuw-van Dalfsen, E., Evers, L. G., & Poland, M. P. (2022). Microgravity Change During the 2008–2018 Kīlauea Summit Eruption: Nearly a Decade of Subsurface Mass Accumulation. *Journal of Geophysical Research: Solid Earth*, *127*(9), Article e2022JB024739. https://doi.org/10.1029/2022JB024739

JGR Solid Earth

RESEARCH ARTICLE
10.1029/2022JB024739

Microgravity Change During the 2008–2018 Kīlauea Summit Eruption: Nearly a Decade of Subsurface Mass Accumulation

M. R. Koymans[1,2], E. de Zeeuw-van Dalfsen[1,3], L. G. Evers[1,2], and M. P. Poland[4]

[1]R&D Seismology and Acoustics, Royal Netherlands Meteorological Institute, De Bilt, The Netherlands, [2]Department of Geoscience and Engineering, Delft University of Technology, Delft, The Netherlands, [3]Department of Geoscience and Remote Sensing, Delft University of Technology, Delft, The Netherlands, [4]U.S. Geological Survey, Vancouver, WA, USA

Key Points:

- Nearly a decade of microgravity campaign data from Kīlauea during its 2008–2018 eruption are analyzed using a weighted least squares approach
- Subsurface mass accumulation between 2009—2015 of order 1.9×10^{11} kg at 1.3 km depth b.s.l. without commensurate surface deformation
- Compression and densification of gas-rich magma may have accommodated increased pressurization in the magmatic system

Supporting Information:

Supporting Information may be found in the online version of this article.

Correspondence to:

M. R. Koymans,
koymans@knmi.nl

Citation:

Koymans, M. R., de Zeeuw-van Dalfsen, E., Evers, L. G., & Poland, M. P. (2022). Microgravity change during the 2008–2018 Kīlauea summit eruption: Nearly a decade of subsurface mass accumulation. *Journal of Geophysical Research: Solid Earth*, *127*, e2022JB024739. https://doi.org/10.1029/2022JB024739

Received 11 MAY 2022
Accepted 22 AUG 2022

Author Contributions:

Conceptualization: M. R. Koymans, E. de Zeeuw-van Dalfsen, M. P. Poland
Data curation: E. de Zeeuw-van Dalfsen, M. P. Poland
Formal analysis: M. R. Koymans
Methodology: M. R. Koymans, M. P. Poland
Resources: E. de Zeeuw-van Dalfsen, M. P. Poland
Software: M. R. Koymans
Supervision: E. de Zeeuw-van Dalfsen, L. G. Evers
Validation: M. R. Koymans
Writing – original draft: M. R. Koymans

Abstract Results from nine microgravity campaigns from Kīlauea, Hawai'i, spanning most of the volcano's 2008–2018 summit eruption, indicate persistent mass accumulation at shallow levels. A weighted least squares approach is used to recover microgravity results from a network of benchmarks around Kīlauea's summit, eliminate instrumental drift, and restore suspected data tares. A total mass of 1.9×10^{11} kg was determined from these microgravity campaigns to have accumulated below Kīlauea Caldera during 2009–2015 at an estimated depth of 1.3 km below sea level. Only a fraction of this mass is reflected in surface deformation, and this is consistent with previously reported discrepancies between subsurface mass accumulation and observed surface deformation. The discrepancy, amongst other independent evidence from gas emissions, seismicity, and continuous gravimetry, indicate densification of magma in the reservoirs below the volcano summit. This densification may have been driven by degassing through the summit vent. It is hypothesized that during the final years of the summit eruption, magma densification resulted in a buildup of pressure in the reservoirs that may have contributed to the lower East Rift Zone outbreak of 2018. The observed mass accumulation beneath Kīlauea could not have been detected through other techniques and illustrates the importance of microgravity measurements in volcano monitoring.

Plain Language Summary Kīlauea, Hawai'i, is one of the best known shield volcanoes in the world. In 2008, a summit eruption began and lasted for over a decade, ending with an outbreak in 2018 from the volcano's lower East Rift Zone (ERZ) that destroyed hundreds of homes. Over the course of the 2008–2018 summit eruption, nine microgravity campaigns were completed around the volcano's caldera. These campaign measurements provide unique insight into mass changes below the surface of the volcano that would not have been detected otherwise. The results show that during 2009–2015, mass was steadily accumulating in the magma reservoirs below Kīlauea's summit. Usually, the accumulation of mass below volcanoes is accompanied by surface inflation, but for Kīlauea it was found that the mass increase was much larger than expected for the observed increase in volume, indicating densification of gas-rich magma in the reservoir. Magma densification may lead to a mass increase without significantly increasing the source volume. The subsequent pressure increase may have contributed to the 2015 summit intrusion and the 2018 lower ERZ eruption.

1. Introduction

Kīlauea, Hawai'i (Figure 1), is one of the most active and accessible shield volcanoes in the world. The volcano provides exceptional opportunities to investigate subsurface magma storage areas and their spatiotemporal evolution. In 2008, a decade-long summit eruption began, characterized by a lava lake that rose and fell according to changes in magma pressure. Effusive activity had also been ongoing since 1983 near the Pu'u'ō'ō vent, 20 km down-rift of the summit on the volcano's East Rift Zone (ERZ). Both eruptions ended suddenly in May 2018, when a dike propagated to the lower ERZ, 40 km down-rift of the summit, erupting over 1 km^3 of material over a period of three months. The outbreak in the lower ERZ left multiple neighborhoods destroyed and was accompanied by piecemeal collapse of Kīlauea's summit (Neal et al., 2019).

The lava lake that was present during Kīlauea's 2008–2018 summit eruption was connected to a shallow magma storage area known as the Halema'uma'u Reservoir (HMMR), centered at 0–1 km depth below sea level (b.s.l.). A second, larger magma reservoir exists beneath the south part of the caldera (Figure 1) centered 2–4 km depth b.s.l. and is referred to as the South Caldera Reservoir (SCR) (Bemelmans et al., 2021; Jo et al., 2015; Lundgren

Writing – review & editing: E. de Zeeuw-van Dalfsen, L. G. Evers, M. P. Poland

et al., 2013; Poland et al., 2014; Wieser et al., 2020). Volume estimates of the HMMR range from 0.2 to 5.5 km^3 (Anderson et al., 2015) and 2.5–7.2 km^3 (Anderson et al., 2019), and the volume of the SCR is thought to exceed 10 km^3 (Poland et al., 2014). The level of the lava lake varied synchronously with ground deformation, indicating a strong—possibly *magmastatic* (a column of magma that is in equilibrium with the deeper pressure)—connection with the HMMR (Anderson et al., 2015; Lundgren et al., 2013; Orr et al., 2015; Patrick, Orr, et al., 2019; Patrick, Swanson, & Orr, 2019; Poland, Carbone, & Patrick, 2021). The connection and interplay between the HMMR and SCR remains uncertain (Anderson et al., 2020; Poland, 2014; Poland, Miklius, et al., 2021; Wang et al., 2021).

Summit eruptive activity between 2008 and 2018 was captured by a diverse set of geodetic observations, including campaign and continuous Global Navigation Satellite System (GNSS), borehole tilt, InSAR, and campaign and continuous microgravity (Poland, Miklius, et al., 2021). Deformation data are an effective tool for investigating changes in subsurface volume and pressure beneath Kīlauea (Bemelmans et al., 2021; Jo et al., 2015); however, only gravity measurements can provide constraints on whether surface deformation is accompanied by subsurface changes in mass—information that is critical for understanding the source of geodetic change (Carbone et al., 2017; Nikkhoo & Rivalta, 2021). Mass accumulation may be a precursor to volcanic activity (Rymer, 1994), making the technique valuable and widely adopted in volcano monitoring to produce quantitative estimates of source characteristics at volcanoes worldwide (Carbone & Greco, 2007; Miller et al., 2017).

1.1. Microgravity Observations at Kīlauea

Over the course of the 2008–2018 eruption, continuous microgravity monitoring near the summit eruptive vent yielded constraints on the density of the lava lake and dynamics of subsurface magmatism. These constraints were based mostly on short-lived signals that spanned minutes to days (Carbone et al., 2013; Carbone & Poland, 2012; Poland & Carbone, 2016, 2018; Poland, Carbone, & Patrick, 2021). In continuous observations from mechanical spring gravimeters, the contributions of instrumental drift and long-term mass changes are challenging to separate. Furthermore, continuous observations from a single location are insufficient to derive quantitative estimates of the location and magnitude of subsurface mass variations. Microgravity campaigns completed over the course of multiple years overcome these limitations by measuring microgravity at a network of benchmarks relative to a reference benchmark that is outside the area of expected gravity change. These measurements, expressed relative to this reference, can be corrected for instrumental drift by repeating the measurements in a short period over which the drift can be quantified and eliminated (Van Camp et al., 2017). Changes in the difference between the benchmarks and the reference benchmark can then be observed over longer periods of time. The increased spatial coverage from microgravity campaigns thus allows the source of long-term subsurface mass variations to be resolved. In campaign gravimetry, however, one challenge is aliasing, meaning that short-duration signals during the campaign may be mistaken for changes occurring over longer periods. Together, continuous and campaign microgravity observations provide unique spatio-temporal constraints on subsurface magma dynamics. It is evident that both types of microgravity data are uniquely valuable in volcano monitoring infrastructure.

Microgravity campaigns began at Kīlauea with sporadic measurements in the 1970s (Jachens & Eaton, 1980; Johnson et al., 2010) and were completed episodically during the 2008–2018 summit eruption using a pair of Scintrex CG-5 gravimeters (Scintrex Limited, 2012). Interpretations based on campaigns completed between 1975 and 2012 suggest significant subsurface mass accumulation below Kīlauea's summit caldera without a commensurate increase in volume, as indicated by a lack of expected surface inflation (Bagnardi et al., 2014; Johnson et al., 2010). The gravity increase has been interpreted as filling of subsurface voids prior to the onset of the summit eruption in 2008 (Johnson et al., 2010), and the densification of gas-rich magma following the start of summit eruptive activity (Bagnardi et al., 2014).

1.2. Microgravity Campaigns and Analysis

Relative spring gravimeters belong to the class of instruments that are sensitive to μGal (1 μGal = 1×10^{-8} m/s^2) variations in the vertical component of gravitational acceleration g, informally referred to as *microgravity*. In campaign gravimetry, this measure of microgravity is expressed relative to another observed value at a reference benchmark called an *anchor*. Portable gravimeters (e.g., Scintrex CG-5 and CG-6, LaCoste and Romberg Model D and G, ZLS Burris instrument) are practical for field surveys due to their compact size and limited weight. Manufacturer specifications for these instruments suggest a resolution of about 1 μGal and standard deviation

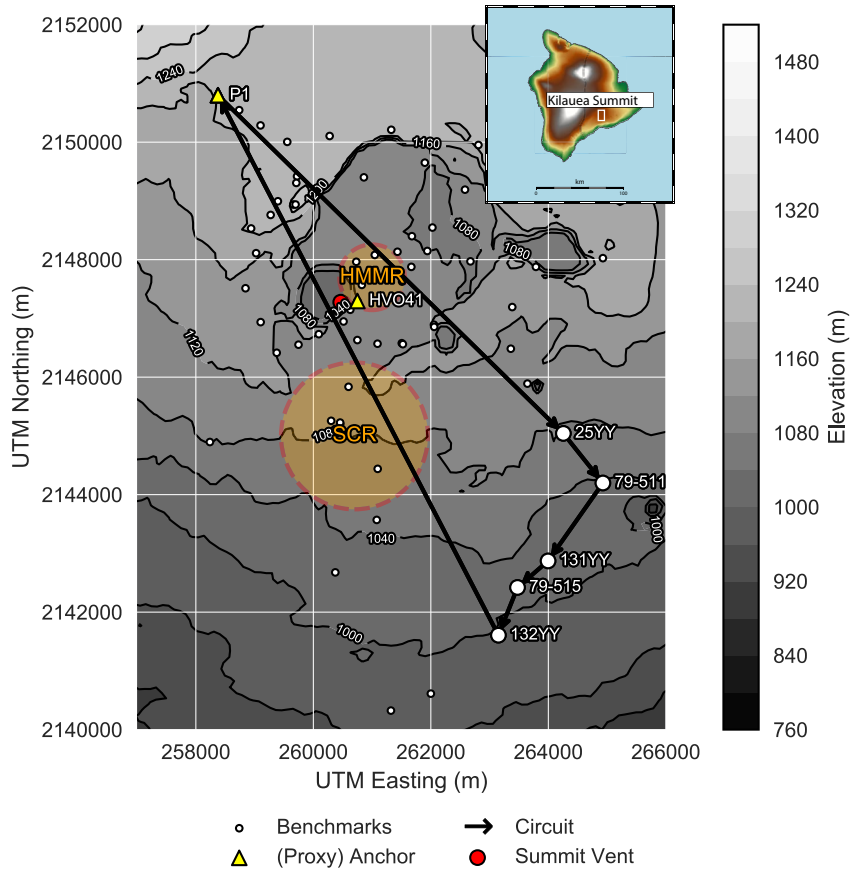

Figure 1. Overview of the summit of Kīlauea, Hawai'i (pre-2018). Each small white circle represents a microgravity benchmark that is made up of a permanently marked site. An example circuit completed on 2010-07-02, visiting a selection of benchmarks (inflated white circles) is illustrated (P1 → 25YY → 79–511 → 131YY → 79–515 → 132YY → P1). After completing a single loop, the circuit is immediately repeated a second time. A list of benchmark identifiers, coordinates, and elevations is supplied with the Supporting Information S1 (Data set S1). The approximate projected surface positions of the Halema'uma'u reservoir (HMMR) and South Caldera reservoir (SCR) are shown following the illustration by Poland, Miklius, et al. (2021).

of 5 μGal for the Scintrex CG-5 (Scintrex Limited, 2012) for repeated measurements. In campaign gravimetry, the term *benchmark* describes a persistent and precise geographical location that is occupied during multiple campaigns. An *occupation* is a single visit to a benchmark during which multiple microgravity measurements are made. During a full campaign that may span days to weeks, multiple *circuits* across a network of benchmarks are completed. Within a circuit, the first measurement is made at the anchor, after which occupations at a number of benchmarks are completed. A high spatial density of benchmarks allows for circuits to be closed, meaning that the anchor is remeasured at the end of each circuit, completing a *loop*. When the same circuit is completed twice, it is referred to as a double loop. The double loop procedure offers insight into measurement repeatability and delivers an important degree of data redundancy. At least one repeated measurement at the network anchor is required to correct for the effect of instrumental drift that is inherent to mechanical spring gravimeters. Data *tares* are sudden and irreversible offsets in gravimeter readings caused by mechanical and/or thermal shocks (e.g., jolting of the instrument by rough transport). This constant offset remains in the data for following occupations. The campaign strategy (Murray & Tracey, 2001) can be chosen based on the network topology with a trade-off between time and data redundancy.

Microgravity differences between the benchmarks and the network anchor are calculated for each campaign and compared between campaigns to extract changes in microgravity over time. Many software packages have been developed to process microgravity data, including for example, GRAVNET (Hwang et al., 2002), MCGravi (Beilin, 2006), gTOOLS (Battaglia et al., 2012, 2022), GravProcess (Cattin et al., 2015), PyGrav (Hector

& Hinderer, 2016), Gsolve (McCubbine et al., 2018), pyGABEUR-ITB (Wijaya et al., 2019), and GSadjust (Kennedy, 2021). The large variety of packages may be a result of lack of standardization in data collection and analysis, particularly due to different strategies to correct for tidal variations and instrumental drift. In this paper, a custom joint weighted least squares (WLS) inversion is adopted to simultaneously solve for instrumental drift and microgravity differences (Hwang et al., 2002; Reilly, 1970). The approach is extended to correct for microgravity offsets introduced by suspected data tares (Koymans, 2022).

In this manuscript, results from nine microgravity campaigns completed between 2009—2017 are presented. The results provide additional constraints on the amount and depth of subsurface mass accumulation beneath the Kīlauea Caldera during its summit eruptive activity.

2. Methodology

At Kīlauea, relative microgravity observations were made during nine campaigns (Flinders et al., 2022) by the United States Geological Survey Hawaiian Volano Observatory (USGS—HVO) between 2009 and 2017 (Figure 2). Each campaign was carried out using two Scintrex CG-5 instruments (serial numbers 578 and 579) for all benchmark occupations. All circuits across the network (Figure 1) were completed as double loops. The benchmark P1 northwest of Kīlauea's summit was used as the network anchor, consistent with previous campaign microgravity studies (Bagnardi et al., 2014; Johnson et al., 2010). For loops that include benchmarks inside Kīlauea Caldera, benchmark HVO41 was sometimes used as a proxy anchor (Figure 1), because logistical constraints made it difficult to return to network anchor P1 between loops. Results from these circuits are therefore expressed relative to the original anchor through another circuit that captures the difference between network anchor P1 and proxy anchor HVO41 on a different day of the campaign. During every occupation at a benchmark, a minimum of five observations were made, where each observation consists of a 60 s measurement sampled at 6 Hz. The resulting 360 samples are averaged to yield a statistical mean and variance per observation.

The microgravity data from all nine campaigns were uniformly analyzed. Initially, clearly erroneous measurements were manually filtered from the data set, including initial observations during each occupation for which the instrument was recovering from transport and converging toward a stable value (Reudink et al., 2014). The period of recovery can last up to 20 min, but data recovered during the settling may still be valuable considering the trade-off between data quality and time. For campaigns where nearby seismic data (HV.NPT.HHZ) (USGS Hawaiian Volcano Observatory (HVO), 1956) were available, microgravity observations distorted by high amplitude inertial signals (e.g., earthquakes) were identified and excluded from processing. Observations with tilts beyond 20″ from vertical and those that were based on fewer than 60 s of recording were removed. The embedded tidal correction applied by the Scintrex CG-5 software (Longman, 1959) was restored to all microgravity observations because of partially erroneous timestamping that propagated to inaccurate tidal corrections in some of the campaigns. The effect of the solid Earth tide was again removed using a branch of Pygtide (Rau, 2018), a Python wrapper for ETERNA 3.4 (Wenzel, 1996). The tidal components were estimated using a global theoretical model following Dehant et al. (1999) as recommended by Van Camp and Vauterin (2005) in the TSOFT manual. The effect of ocean loading was removed using parameters obtained from the free ocean loading provider (Bos & Scherneck, 2014) using the TPXO9-atlas (Egbert & Erofeeva, 2002). The tidal constituents returned from the provider were evaluated using the International Earth Rotation and Reference System Service standard program HARDISP (Agnew, 2010).

During a single circuit spanning a period of hours, instrumental drift of the CG-5 can be characterized by a monotonic linear function. The instruments implement an automated drift correction, but a residual drift always remains to be considered. A WLS inversion was used to find a solution for the gravity differences with the anchor and linear instrumental drift parameters (Hwang et al., 2002), including any offsets introduced by suspected data tares (Koymans, 2022). An example solution for a single circuit is illustrated in Figure 3. A detailed derivation of the microgravity analysis and uncertainty estimation is provided with the Supporting Information S1 (Text S1).

2.1. Deformation Correction

InSAR data were acquired by the X-band TerraSAR-X and COSMO-SkyMed satellite systems (Table 1). Data were processed using the GAMMA software (Werner et al., 2000), with the topographic correction made using a 5 m digital elevation model (Poland, 2014). Satellite line-of-sight displacement vectors $\mathbf{U}^*$ were calculated from unwrapped interferograms $\mathbf{U}$ following the same approach as Bagnardi et al. (2014). The satellites are, by

Journal of Geophysical Research: Solid Earth
10.1029/2022JB024739

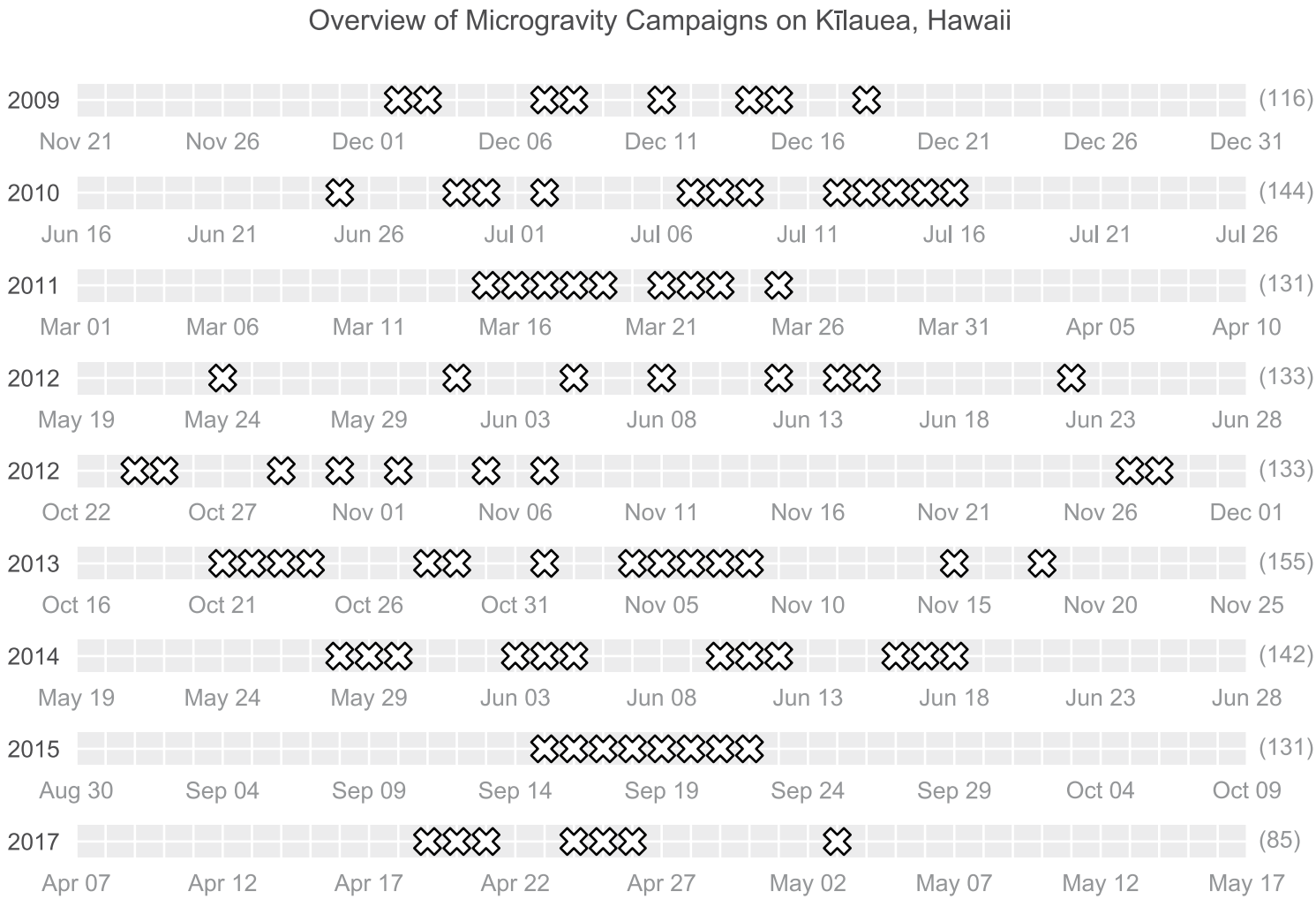

Figure 2. Overview of relative microgravity campaigns on Kīlauea, Hawai'i between 2009 and 2017. The rows span 41 days and each white marker represents a single day on which a circuit across the network was conducted. The number in parenthesis on the right is equal to the number of occupations made during the campaign. A total of nine campaigns were completed with a total of 87 days spent in the field.

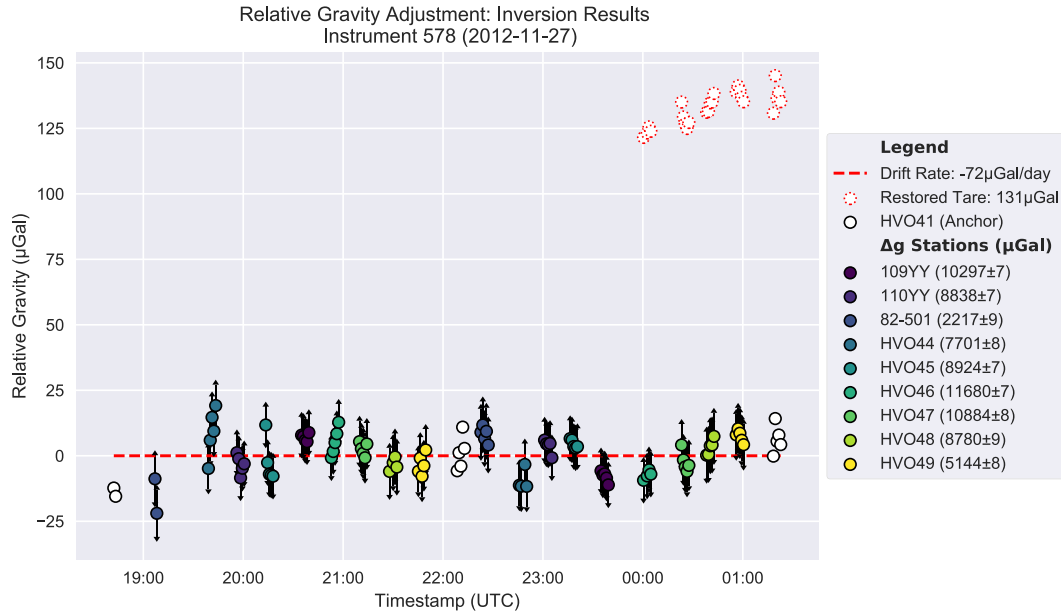

Figure 3. Observations from a single campaign day (2012-11-27) for Scintrex CG-5 578 on Kīlauea, Hawai'i. The vertical error bars illustrate the 95% confidence interval for the recovered gravity differences with the anchor. Proxy anchor HVO41 has no confidence interval because the data are kept fixed during the inversion. Solutions for the gravity differences with the anchor (subtracted from observations) and linear instrumental drift (corrected) are shown. The magnitude of the recovered microgravity differences and uncertainties are given in the legend. The residual daily linear drift rate is estimated at −72 μGal/d. An additional degree of freedom that represents a data tare was added to the inversion for the group of data marked in red. This tare was restored during the inversion with an offset of 131 μGal.

approximation, characterized by north-to-south orbital trajectories, with a heading that is off by a maximum of a few degrees. By this approximation, the line-of-sight displacement vectors from the ascending and descending tracks can be decomposed to a horizontal (east to west) and vertical component (Yun et al., 2006):

$$\begin{bmatrix} \mathbf{U}^*_{\text{descending}} \\ \mathbf{U}^*_{\text{ascending}} \end{bmatrix} = \begin{bmatrix} \sin(\lambda_1) & \cos(\lambda_1) \\ -\sin(\lambda_2) & \cos(\lambda_2) \end{bmatrix} \begin{bmatrix} \mathbf{U}_z \\ \mathbf{U}_h \end{bmatrix} \quad (1)$$

Where $\mathbf{U}^*$ represents the vector of line-of-sight displacement for the respective trajectory, and λ_1 (descending) and λ_2 (ascending) the corresponding satellite incidence angles measured from horizontal. Given the line-of-sight displacements for the ascending and descending trajectory, Equation 1 can be used to find solutions for the vertical ($\mathbf{U_z}$) and horizontal (east to west) ($\mathbf{U_h}$) deformation. Despite the occasional mismatch in temporal

Table 1
Satellites and Temporal Coverages Used for InSAR Vertical Deformation Estimates

		Descending track			Ascending track		
Epoch	X band satellite	Start date	End date	λ_1 (°)	Start date	End date	λ_2 (°)
2009–2010	TerraSAR-X	2009-12-04	2010-06-09	31.2	2009-12-05	2010-06-09	33.2
2010–2011	TerraSAR-X	2010-06-09	2011-04-02	31.2	2010-06-10	2011-04-03	33.2
2011–2012	COSMO-Skymed	2011-03-10	2012-05-15	41.5	2011-03-11	2012-05-28	38.8
2012–2012	COSMO-Skymed	2012-05-15	2012-10-30	41.5	2012-05-20	2012-10-23	38.8
2012–2013	COSMO-Skymed	2012-10-30	2013-12-04	41.5	2012-10-23	2013-11-27	38.8
2013–2014	COSMO-Skymed	2013-11-02	2014-05-29	41.5	2013-10-26	2014-06-20	38.8
2014–2015	COSMO-Skymed	2014-05-29	2015-09-06	41.5	2014-06-20	2015-09-02	38.8
2015–2017	COSMO-Skymed	2015-09-06	2017-04-23	41.5	2015-09-11	2017-04-16	38.8

coverage, ascending and descending interferograms are acquired within a few days of one another. Furthermore, the interferograms span months to years and were chosen without overlap with respect to known major deformation events, like the 2011 Kamoamoa fissure eruption (Lundgren et al., 2013) and 2015 summit intrusion (Bemelmans et al., 2021; Jo et al., 2015). Vertical deformation data were smoothed using a median filter over an area of roughly 100 m.

Vertical deformation estimates from InSAR data were constrained by continuous GNSS data by minimizing the squared residual between the InSAR and GNSS data at the GNSS station locations. Estimates of the vertical position of 12 GNSS stations over the periods that match the InSAR acquisition dates were manually interpolated from the plotted time-series data (Figure S2 in Supporting Information S1).

The amount of vertical deformation at each benchmark was estimated for the InSAR acquisition dates that closely match the microgravity campaigns. The recovered change in height for each benchmark relative to network anchor P1 was converted to gravity assuming a theoretical free-air gradient of −308 μGal/m (Fowler et al., 1990). Measured local gradients of −327.3 μGal/m (Johnson, 1992) and −330.25 μGal/m (Kauahikaua & Miklius, 2003) are close to this theoretical estimate and should not significantly influence the results (Bagnardi et al., 2014; Johnson et al., 2010) when deformation remains limited to a maximum of tens of centimeters.

2.2. Point Source Inversion

Observed microgravity changes that were corrected for vertical deformation can be inverted to recover best-fit point source parameters. These sources are described by a change in subsurface mass and associated position. This geometry has proven to be a suitable approximation for microgravity change sources at Kīlauea's summit in previous studies (Bagnardi et al., 2014; Johnson et al., 2010; Poland et al., 2019) and is often used to model the HMMR (Anderson et al., 2015; Bemelmans et al., 2021; Lundgren et al., 2013; Poland et al., 2014).

For a point source, the vertical change in gravity (δg_i) at the ith benchmark in the Kīlauea network can be approximated by:

$$\delta g_i = \mathrm{G}\delta m \frac{(\delta z - z_i)}{r^3} - \delta g_{\mathrm{P1}} \tag{2}$$

Where $G = 6.674 \times 10^{-11}$ m^3 kg^{-1} s^{-2} is the universal gravitational constant, δm the change in mass, and $r = \sqrt{(\delta x - x_i)^2 + (\delta y - y_i)^2 + (\delta z - z_i)^2}$ equals the Euclidean distance between the benchmark position (x_i, y_i, z_i) and the inferred point source location (δx, δy, δz). The term δg_{P1} accounts for the predicted effect of the point source felt at the anchor location and can be found by recursive application of Equation 2. The squared residual between the modeled and observed changes in gravity difference is minimized with respect to the four variable point source parameters (δm, δx, δy, δz) using the Powell method (Powell, 1964) implemented in SciPy (Virtanen et al., 2020). The point sources and gravity residuals were calculated from the average gravity changes of the CG-5 instruments in order to maximize the gravity signal-to-noise ratio. Three benchmarks near the summit eruptive vent (HOVL-G, HVO41, and 205YY) that are strongly influenced by variations in the lava lake level were excluded from the inversion.

An estimate for confidence intervals on the source inversion results is made through a parametric bootstrap ($n = 5{,}000$) by sampling the standard deviation of the microgravity changes. From this ensemble of point source solutions, the bottom and top 2.5% parameter estimates are discarded, resulting in discrete 95% confidence interval for the point source parameters (δm, δx, δy, δz), including the median of the ensemble of bootstraps.

3. Results

The results from the full vertical deformation and microgravity analysis are summarized in Figure 4. A tabular compilation of microgravity analysis results, as well as vertical displacement estimates at each benchmark are included in the Supporting Information S1 (Data set S1).

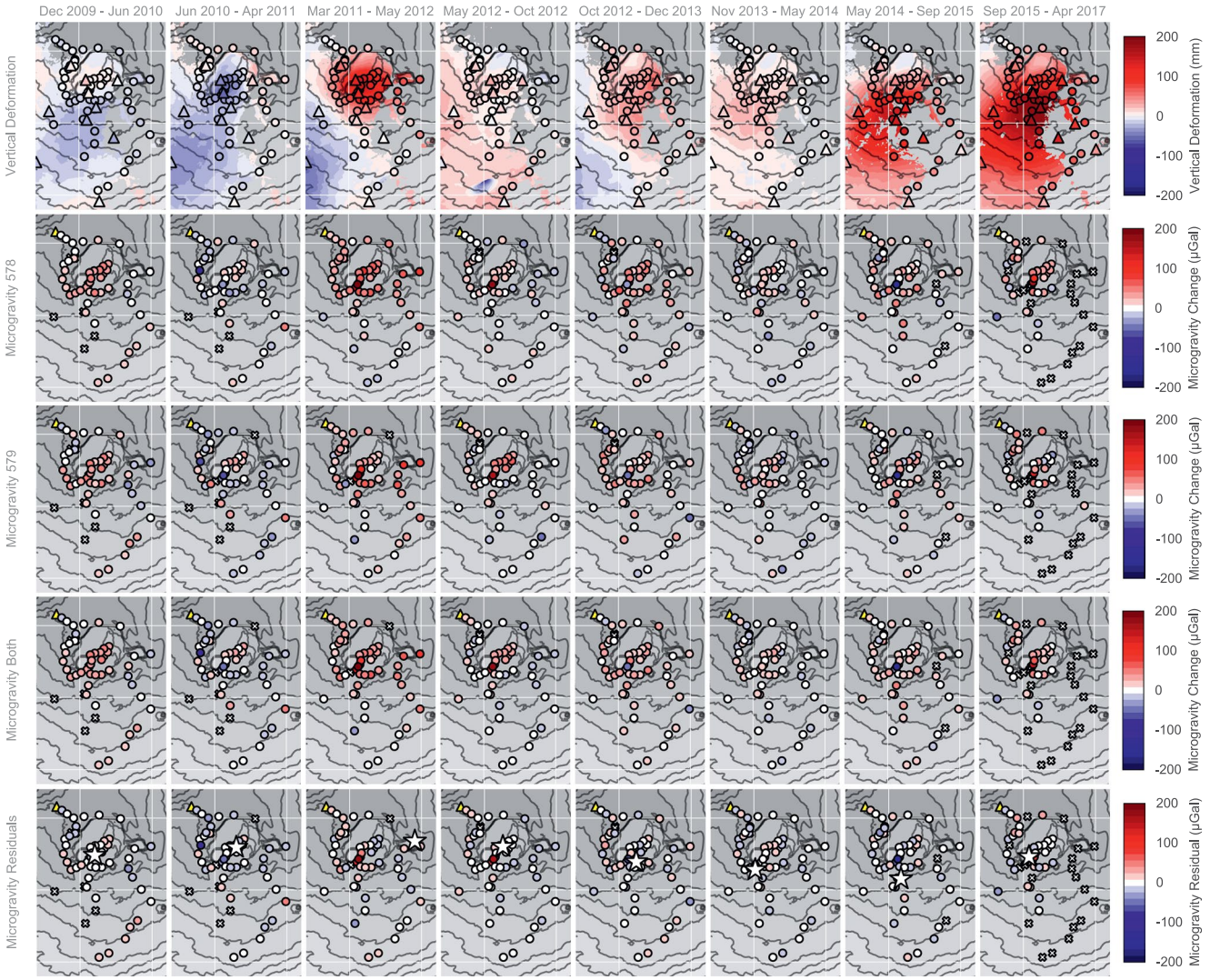

Figure 4. Columns represent the period between two consecutive microgravity campaigns on Kīlauea, Hawai'i. (Row 1) vertical deformation (triangles = Global Navigation Satellite System receivers, circles = benchmarks), (Rows 2 and 3) gravity changes corrected for vertical deformation for instruments 578 and 579 respectively (triangle = anchor P1, circles = benchmarks, cross = missing). (Row 4) average gravity changes for instruments 578 and 579. (Row 5) inverted point source solutions and microgravity residuals after correcting for the source (star = source location). The spatial coverage of the panel frames is identical to Figure 1 and omitted to save space.

3.1. Vertical Deformation

The vertical displacement maps in the first row of Figure 4 illustrate vertical deformation estimates from the InSAR data that were constrained by the continuous GNSS stations. The vertical displacement from the InSAR data at each microgravity benchmark is shown for comparison. Vertical deformation captured by GNSS and InSAR is consistent within 1–2 cm (≈3 to 6 μGal), well within the typical 20 μGal uncertainty of microgravity change derived from campaign measurements (Poland & de Zeeuw-van Dalfsen, 2019).

Between 2009 and 2010 (Figure 4—row 1, panel 1), a maximum of 3 cm of subsidence occurred south of Kīlauea Caldera, with a negligible amount of deformation within the caldera itself. The subsidence trend continued into 2011, with the 2010–2011 period seeing up to 5 cm of subsidence in the center of the caldera (Figure 4—row 1, panel 2). From March 2011 to June 2012, deformation in the caldera was characterized by uplift of up to 15 cm focused on the center of the caldera, while the south part of the caldera remained relatively stable (Figure 4—row 1, panel 3). Over the course of mid to late 2012, no substantial deformation was identified at Kīlauea's summit (Figure 4—row 1, panel 4). Between 2012 and 2014, slow summit uplift began in the caldera center which

migrated toward the south (Figure 4—row 1, panels 5 and 6). After 2014, uplift occurred across the summit region but was mainly centered south of the caldera, with uplift rates exceeding 10 cm/yr (Figure 4—row 1, panels 7 and 8) above the expected position of the SCR. The progression of deformation is consistent with GNSS time series that illustrate an overall transition from subsidence to uplift over the course of the 2008–2018 summit eruption, interrupted by occasional transient displacements caused by summit and ERZ intrusions and eruptions (Poland, Miklius, et al., 2021).

3.2. Microgravity

The panels presented in Figure 4 rows 2 and 3 illustrate microgravity results corrected for vertical deformation at all benchmarks for instruments 578 and 579 respectively.

Between December 2009 and June 2010 (Figure 4—rows 2 and 3, panel 1), an increase in gravity on the order of tens of μGals in the center of the caldera is apparent in data from both gravimeters. There is no coherent pattern from either gravimeter in the subsequent epoch spanning June 2010 to March 2011 (Figure 4—rows 2 and 3, panel 2). A major decrease of approximately 70 μGal during this epoch occurs at a benchmark on the western flank of Kīlauea. This feature is expressed in both instruments but is not representative of the wider area, indicating a local effect or measurement artifact. An increase of similar magnitude happens at a single benchmark to the southeast. From March 2011 to June 2012 (Figure 4—rows 2 and 3, panel 3), an increase in gravity (50–200 μGal) appears near the summit eruptive vent and the general region near the center of Kīlauea Caldera, stretching toward Kīlauea Iki crater and to the southeast. The increase in microgravity is largest at the benchmark in closest proximity to the lava lake (HOVL-G), and similarly elevated for two nearby benchmarks (205YY, and HV041). In data spanning mid to late 2012 (Figure 4—rows 2 and 3, panel 4), the gravity increase near the lava lake persists, with almost all variation (100–200 μGal) happening in the vicinity of the eruptive vent. No further significant changes in gravity can be identified during this period for instrument 578, but instrument 579 is characterized by a large increase (40–60 μGal) inside Kīlauea Caldera. Between November 2012 and 2013 (Figure 4—rows 2 and 3, panel 5), a gravity increase occurred in Kīlauea Caldera, showing a pattern that is similar in spatial extent and magnitude as that from December 2009 to June 2010. Very little change in gravity can be observed during 2013–2014 (Figure 4—rows 2 and 3, panel 6). Between June 2014 and September 2015 (Figure 4—rows 2 and 3, panel 7), the most noteworthy gravity change is a 150 μGal decrease near the summit eruptive vent. The results from 2015 to 2017 (Figure 4—rows 2 and 3, panel 8) are limited in the number of available benchmarks and appear inconclusive, but data from instrument 578 indicate an increase in gravity nearest to the summit vent, with little to no change elsewhere. Row 4 of Figure 4 illustrates the average of both instruments and was used as input data for the point source inversions.

Results from the entire period spanning December 2009 to April 2017 are mainly characterized by a persistent increase in gravity that radiates outward from the center of Kīlauea Caldera. The gravity variations with the largest amplitude are observed at the benchmarks near the summit eruptive vent (HOVL-G, HVO41, and 205YY) and closely follow the level of the rising and falling lava lake (Figure 8).

3.2.1. Differences Between Gravity Meters CG-5 578 and 579

The comparison of microgravity results for the two instruments in Figure 4—rows 2 and 3, illustrates that there is variation in what two different gravimeters record. Even though the instruments have been subjected to the same conditions and modes of transport. However, when considering the confidence limits on the mean gravity difference (15–20 μGal) that include operator and environmental noise, the instruments generally occupy the same range. The gravity residuals from the linear drift model for each circuit are presented in Figure 5. The residuals approximate a normal distribution, indicating that the applied drift model is appropriate. Uncertainties on the mean gravity differences are on the order of a few to a few tens of μGal, depending on the instrument, campaign, and circuit. One implication of the residuals is that gravity changes derived from campaign measurements at Kīlauea cannot be resolved with confidence below approximately 20 μGal. Based on merit of its lower residuals, instrument 578 outperformed instrument 579 (Figure 5). Instrument 579 was in fact found to be unreliable in campaigns at Yellowstone during 2017 (Poland & de Zeeuw-van Dalfsen, 2019). These campaigns exposed instrumental problems that may also have been present earlier and could explain the discrepancy between the two instruments observed in the 2015 and 2017 measurements at Kīlauea. This deterioration is not clearly expressed in the gravity residuals in Figure 5; however, such residuals would not capture constant offsets from

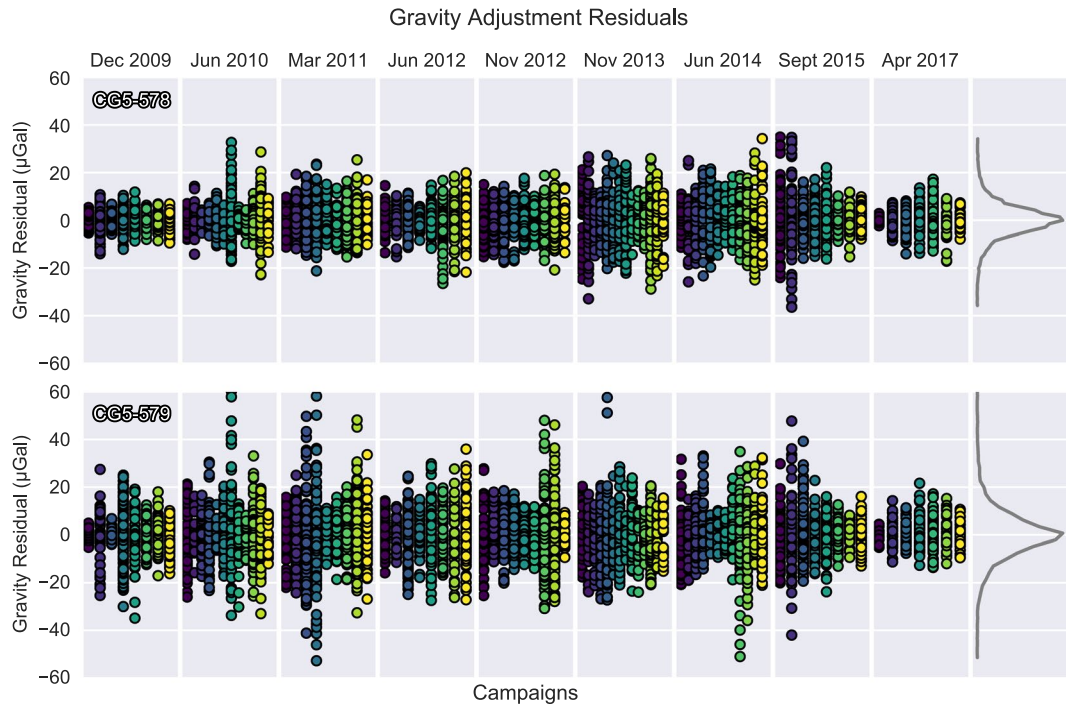

Figure 5. Microgravity residuals from the estimated linear drift model for instruments 578 (top) and 579 (bottom) for all campaigns and circuits on Kīlauea, Hawai'i. Each consecutive circuit in a campaign is given a distinctive color and a new entry on the *x*-axis. In the ideal case where the model fits the observations the residuals of each circuit should be normally distributed. Deviations from this behavior may indicate problems with the applied linear drift model, instruments, or the measurements themselves. The right-most panels show histograms of the residuals, illustrating a tighter distribution on instrument 578 compared to 579.

for example, calibration errors that affect the mean microgravity results. Furthermore, single loops were more commonplace in the 2017 campaign, effectively producing lower residuals but definitely not more reliable data. The instruments were calibrated against absolute measurements on a line at Mount Hamilton, California. The instrument calibration factors did not change between the 2009–2017 campaigns, but it was apparent from calibration line measurements that instrument 579 needed servicing in late 2017 (Battaglia et al., 2018).

3.3. Recovered Point Source Solutions

Solutions and bootstrapped parameter estimates are summarized in Table 2 and Figure 4—row 5 and Figure 6. In the following paragraphs the results are discussed by epoch:

- *December 2009 to June 2010* (Figure 4—row 5, panel 1) shows a shallow source at 500 m depth b.s.l. toward the northeast of Halema'uma'u crater with a mass change on the order of 2.0×10^{10} kg. The parameter estimates in Figure 6 follow Gaussian distributions with tight confidence bounds on the median of the parameter estimates. The location of the point mass is consistent with the observed radial pattern of gravity changes presented in Figure 4.
- *June 2010 to March 2011* (Figure 4—row 5, panel 2) resolves to a very shallow depth, with an order of magnitude less mass addition compared to the previous epoch. The distribution of bootstrapped parameters appears skewed and may be attributed to the absence of large and coherent gravity changes during this period.
- *March 2011 to June 2012* (Figure 4—row 5, panel 3) initially resolved to a greater depth and mass addition than preceding epochs. Its resolved location is toward the northeast of Kīlauea Caldera at a location where no large mass change is expected (illustrated in Figure 4). Therefore the horizontal position of the point source was kept fixed at the approximated surface location of the center of the HMMR (261000, 2147500) and the change in mass for this source becomes 1.1 to 1.6×10^{11} kg at 2.4–2.9 km depth b.s.l. The fixed point source is not illustrated in Figure 4 but its resolved parameters are provided in Table 2.

Table 2
Median of the Point Source Inversion Parameters for all Periods Between Microgravity Campaigns at Kīlauea, Hawai'i

	Inverted source parameters			
Campaign period	Mass (kg)	UTM easting (m)	UTM Northing (m)	Depth b.s.l. (m)
December 2009–June 2010	2.0×10^{10}	261,000	2,147,400	0.5×10^{3}
June 2010–March 2011	1.3×10^{9}	261,500	2,148,000	-0.6×10^{3}
March 2011–June 2012	2.2×10^{12}	264,500	2,148,500	9.1×10^{3}
March 2011–June 2012*	1.3×10^{11}	261,000	2,147,500	2.6×10^{3}
June 2012–November 2012	5.6×10^{9}	261,200	2,148,000	-0.2×10^{3}
November 2012–November 2013	7.8×10^{10}	261,200	2,147,000	2.5×10^{3}
November 2013–June 2014	1.2×10^{10}	260,100	2,136,400	1.0×10^{3}
June 2014–September 2015	9.5×10^{10}	260,900	2,145,800	3.5×10^{3}
September 2015–April 2017	1.2×10^{10}	260,400	2,147,300	-0.2×10^{3}
Overall Period				
December 2009–September 2015	1.9×10^{11}	261,200	2,147,400	1.3×10^{3}

Note. The discrete 95% confidence intervals are illustrated in Figure 6. The entry marked by an asterisk (*) had its surface location kept fixed. The given depths are expressed relative to sea level (b.s.l. = below sea level). The surface elevation of the Kīlauea Caldera floor is approximately 1,100 m.

- *June 2012 to November 2012* (Figure 4—row 5, panel 4) shows a modeled source located toward the center of Kīlauea Caldera. This result is mostly influenced by the data from instrument 579. The ensemble of point sources resolve with Gaussian bootstrapped confidence intervals at shallow depth with little mass change.
- *November 2012 to November 2013* (Figure 4—row 5, panel 5) resolves below Kīlauea Caldera, with a mass change of approximately 7.8×10^{10} kg at 2.5 km depth b.s.l. The gravity increase for this period appears to decrease with distance from the source, and the inversion provides a robust point source solution.
- *November 2013 to June 2014* (Figure 4—row 5, panel 6) shows multiple peaks in the parameter distributions. The optimization thus recovers multiple stable point sources (bi-modality in Figure 6), particularly with a depth and mass trade-off. Surface microgravity observations cannot distinguish between an increase in depth or decrease in mass. This may result in multiple distributions of point sources representing greater depth and mass versus shallower depth and smaller mass.
- *June 2014 to September 2015* (Figure 4—row 5, panel 7) indicates a point source at greater depth and larger increase in mass than preceding epochs.
- *September 2015 to April 2017* (Figure 4—row 5, panel 8) expressed bi-modal behavior in terms of mass and depth and cannot be reliably resolved. The poor quality of the 2017 campaign and lack of coherent gravity changes for this period make the result unsurprisingly inconclusive.

All modeled point sources indicate mass increase beneath Kīlauea Caldera. Because of the low signal-to-noise ratio of the microgravity observations, results from changes between adjacent campaigns are often inconclusive. To provide a more robust estimate, the gravity changes are integrated over the period spanning December 2009 to September 2015 (omitting the poor 2017 campaign). This point source solution is represented by a mass increase of $1.6–2.4 \times 10^{11}$ kg at a depth of 1.0–1.7 km b.s.l. beneath the center of the caldera, with Gaussian and narrow confidence intervals (Figure 7). The recovered horizontal location is consistent with that of the shallow HMMR, but at slightly greater depth, indicating that perhaps the base of the reservoir is a dominant region of mass accumulation beneath Kīlauea Caldera—a result similar to previous studies (Bagnardi et al., 2014; Johnson et al., 2010; Poland et al., 2019). The additional results presented here demonstrate that mass accumulation proceeded even during the later stages of the 2008–2018 eruption.

4. Discussion

The analysis of multiple microgravity campaigns at the summit of Kīlauea spanning 2009–2017 provides a foundation for understanding the dynamics of subsurface magmatism, as well as strategies for optimizing the quality and utility of campaign gravimetry. One of the current challenges in terrestrial microgravity

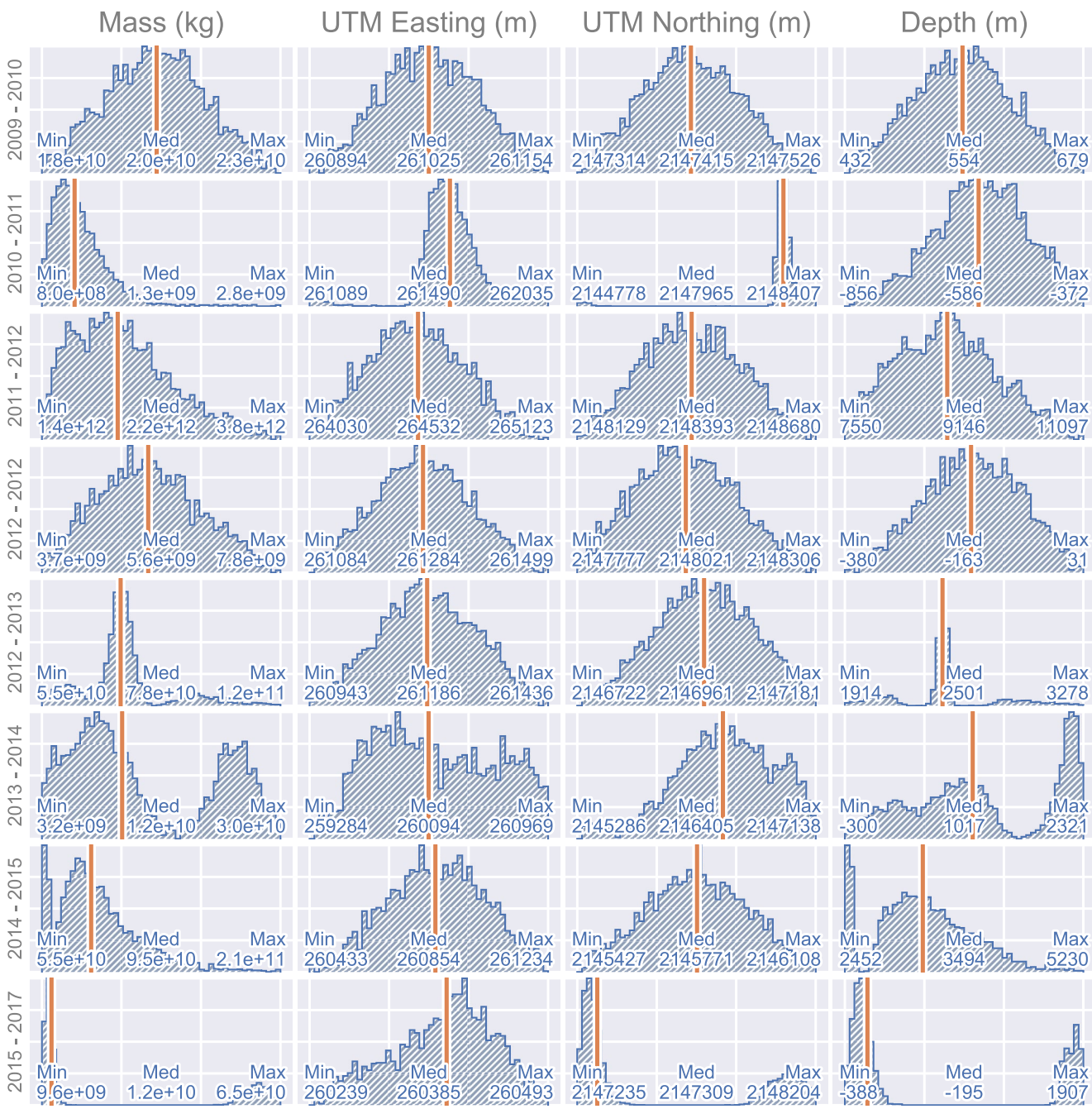

Figure 6. Histograms showing the parameter distributions of 5,000 bootstrapped inverted point sources for microgravity campaigns on Kīlauea, Hawai'i for the indicated time periods in Table 2. The lower 2.5% and upper 97.5% discrete percentiles are given as confidence bounds on the median value and define the boundary of the histograms. The median (med) value is represented by the vertical orange bar.

exists in increasing the spatio-temporal resolution of data. It is evident that campaign gravimetry is mainly limited by its temporal resolution and high uncertainties caused by often unquantified external effects. This limitation is not inherent to the technique but mainly imposed by high instrumental cost and the time and personnel needs of microgravity campaigns. Projects that aim to surmount these challenges are currently being undertaken (Carbone et al., 2020) by utilizing arrays of low-cost Microelectromechanical System gravimeters (Middlemiss et al., 2016).

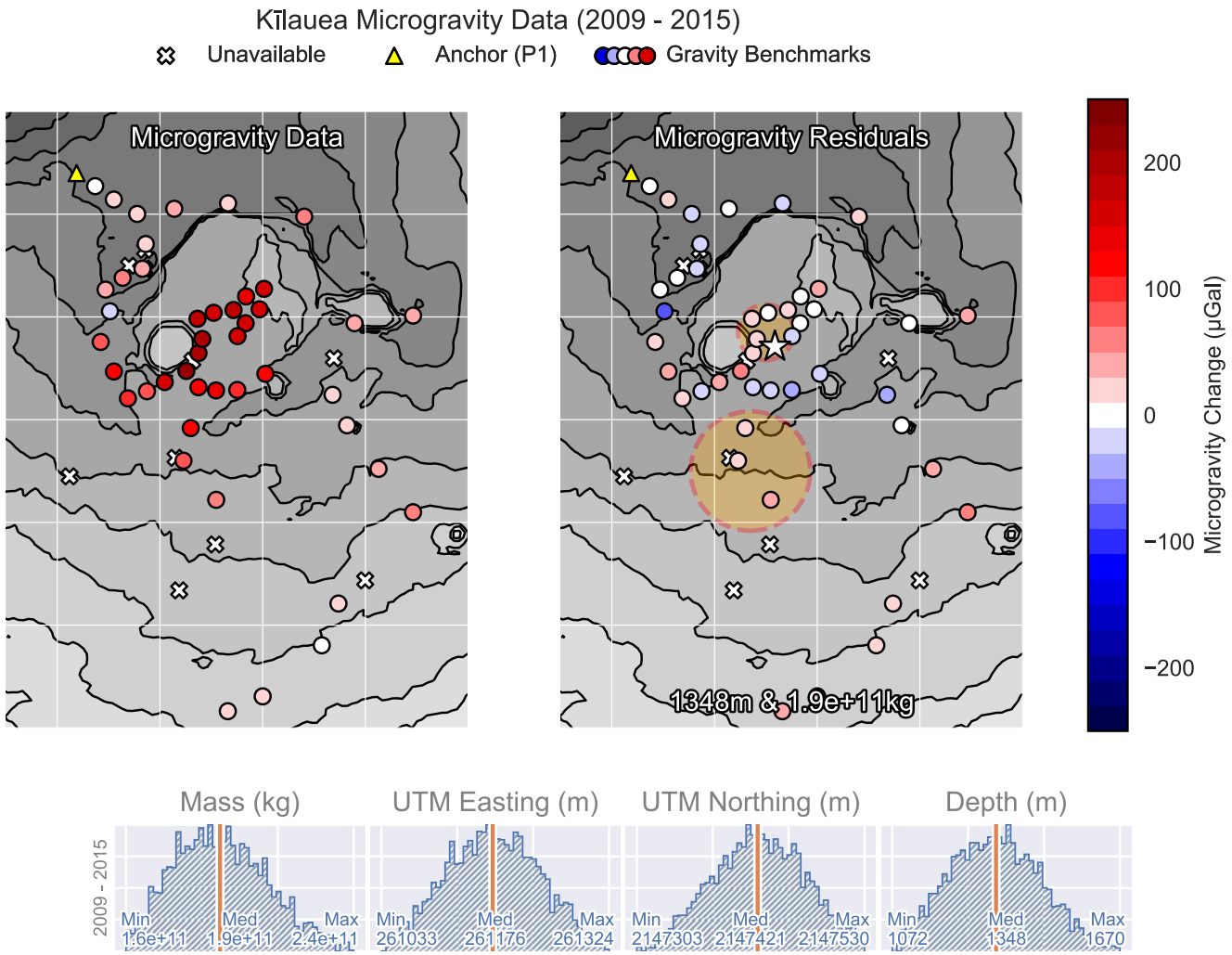

Figure 7. Maps showing the observed gravity changes (left) and inferred point source location and remaining gravity residuals (right) between December 2009 and September 2015 on Kīlauea, Hawai'i. The yellow triangle represents network anchor P1, and benchmarks for which data is missing are marked by a white cross. The location of the inverted point source is illustrated by a star, with an annotation for the associated mass and depth at the bottom. The bootstrapped parameter estimates are shown in the bottom row of panels. The spatial coverage and surface reservoir projections are equivalent to Figure 1.

4.1. Campaign Strategy and Network Adjustment Method

This work demonstrates the effectiveness of a WLS inversion (Hwang et al., 2002) to recover relative gravity differences from double-looped circuits. By utilizing this approach, data tares can be automatically restored when the group of data affected by the tare is known (Koymans, 2022). Furthermore, instead of using the mean of an occupation, individual measurements are used in the WLS inversion. As a result, the observed drift during a single occupation (which can be up to 1 μGal/min) contributes information to the solution. Finally, an inaccuracy in the solid Earth tide or ocean loading models may not entirely prevent residual higher-order harmonic signals from being present in the measurements. In a circuit that spans up to 12 hr, a second- or third-order polynomial may help eliminate any residual (harmonic) components. The linear drift correction in the WLS can be trivially extended to correct for higher-order trends (Koymans, 2022). Higher-order trends could be identified in a preliminary attempt with a linear drift and subsequently assessing the residuals from this linear model. When the gravity residuals from a linear drift model are large, a higher-order polynomial can be tried instead. However, with an insufficient number of occupations a high-order trend may tend to over-fit the data and be detrimental to the results. For this reason, all circuits presented in this manuscript were fitted with a linear drift model.

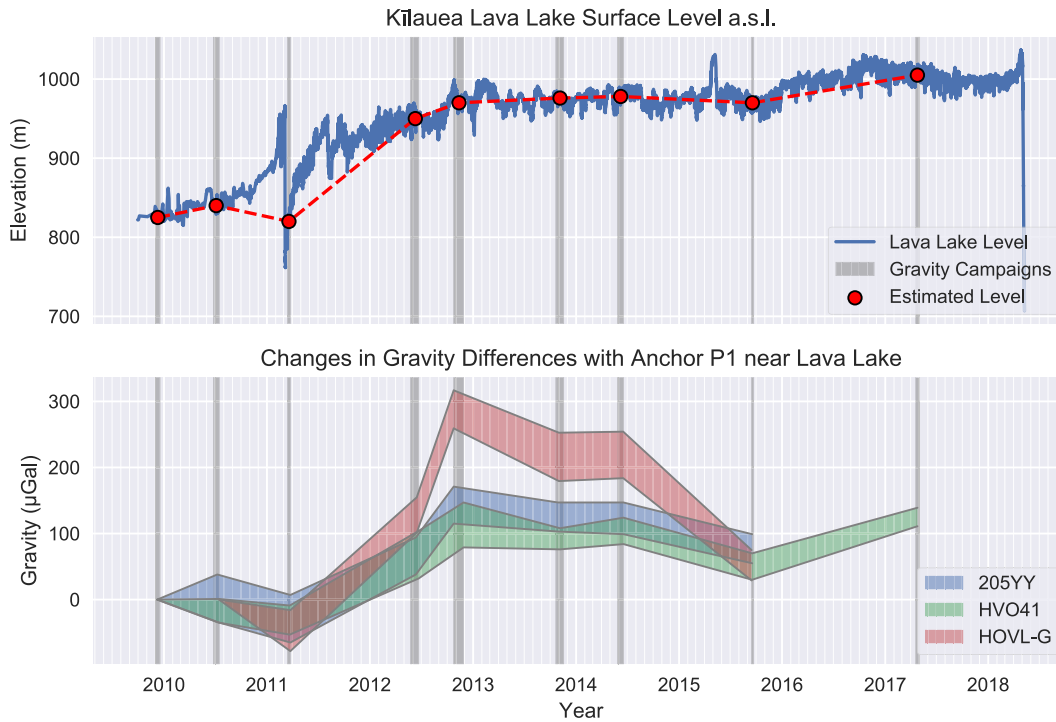

Figure 8. (Top) Absolute Kīlauea lava lake levels from sea level between 2010 and 2018 on Kīlauea, Hawai'i (Patrick, Swanson, & Orr, 2019). The time spans of the microgravity campaigns from Figure 2 are marked by vertical gray bars. Bottom) Observed changes in gravity difference of three benchmarks closest to the lava lake (HOVL-G, 205YY and HVO41) with confidence ranges. The data have been corrected for the contribution of the recovered point source solutions (Table 2). Since 2011, the level has been steadily rising outside of a major disruptive event at Kamoamoa in the beginning of 2011. Beyond 2013 the level of the lake remained stable besides the 2015 summit intrusion, until ultimately draining completely after the outbreak in the lower East Rift Zone (ERZ) in 2018. a.s.l. = above sea level.

4.1.1. Single Versus Double Closed Loops

A single occupation (composed of multiple observations) from a benchmark, as during a single-loop circuit, when presented with a degree of freedom, will always align itself with the imposed drift model. When at least two occupations of a benchmark (taken with hours in between) align with the drift model, confidence in the result increases significantly. This means that multiple occupations of a benchmark provide important insight into measurement repeatability. A single loop is always insufficient because a tare in the data may be misinterpreted as instrumental drift. The presence of tares (listed in the Supporting Information S1) appears relatively common, with a total of 14 suspected tares observed (offsets between 20 and 130 µGal) over all the Kīlauea campaigns for both instruments combined. The effect of occasionally completed single loops becomes most apparent in the campaigns from 2017, which have low coherence between instruments and relatively poor data quality. Due to the inherently low repeatability of microgravity measurements, a certain degree of data redundancy is always recommended. Double loops are clearly favorable in environments that are characterized by significant ambient noise and where rough transport of the instruments cannot be avoided. A key challenge is finding the right balance in the trade-off between effort and data quality, but a minimum of two occupations at each benchmark is needed for reliable results.

The advantage of repeating occupations with multiple instruments is evident from the results and can also assist with the detection of data tares. The presented discrepancies between instruments 578 and 579 emphasize that is it especially valuable when the instruments can be cross-calibrated against an absolute reference before being used in the field (Miller et al., 2017).

4.1.2. Pitfalls of (Proxy) Anchors

Besides instrumental calibration errors, a systemic bias is introduced to the results when microgravity changes occur at the network anchor. An absolute measurement of microgravity may be used to rule out such changes

(Van Camp et al., 2017), but was not available for the presented Kīlauea microgravity campaigns. Because the network anchor P1 is located at a site away from volcanic activity, no significant microgravity change or bias in the results is expected, nor observed in Figure 4 that would appear as a consistent increase or decrease in all benchmarks.

An important recommendation based on the microgravity results from Kīlauea is to consistently measure all benchmarks in a direct circuit with the network anchor. Each measurement in a circuit has an associated uncertainty and when expressed through a proxy anchor, as was done for some occupations at benchmarks inside Kīlauea Caldera, the uncertainties of both measurements are compounded. More importantly, transient gravity changes caused by variations in the lava lake level affect proxy anchor HVO41. Because the lava level can vary over time scales of hours to days (Patrick, Swanson, & Orr, 2019), it is possible that the lava lake level will induce significant differences in gravity at HVO41 on the day that it is used as a proxy anchor for caldera-floor benchmarks compared to the day that it is tied to network anchor P1. In this situation, a bias is introduced when benchmarks originally measured relative to proxy anchor HVO41 are expressed relative to network anchor P1. This complication may explain some of the microgravity-change results between 2010 and 2011, where the observed gravity increase in Kīlauea Caldera (Figure 4—rows 2–4, panel 2) may be attributed to the sudden rise in the lava lake level in 2011 over two days. Similarly, a single poor measurement between network anchor P1 and proxy anchor HVO41 may also explain the anomalous increase in Kīlauea Caldera for instrument 579 between June and November 2012 (Figure 4—row 3, panel 4). These artifacts of the campaign strategy may explain why measurements on the caldera floor appear consistently higher during this period, and those data should be interpreted with caution in terms of the modeled source mechanisms. It naturally follows that an overestimation in one campaign would result in an underestimation in the next. Proxy anchors that are subject to high noise and transient microgravity effects should be avoided whenever possible.

4.2. Uncertainties in Campaign Gravimetry

Relative microgravity measurements are subject to many sources of uncertainty (Giniaux et al., 2017; Poland & de Zeeuw-van Dalfsen, 2019; Van Camp et al., 2017) and are notoriously difficult to interpret. Microgravity campaigns should ideally be completed at regular intervals (e.g., monthly or yearly) and not just in response to disruptive and transient events. All sources of microgravity change between two campaigns are integrated into a single estimate, making it challenging to isolate individual contributions and processes. This is especially problematic when the measurement is integrated over multiple years, and includes nearby disruptive events such as the 2015 summit intrusion that change the gravity field through the emplacement of mass and associated deformation. Seasonal and hydrological effects, such as rain and snow melting, may induce significant subsurface mass changes (Carbone et al., 2019; Miller et al., 2017; Poland & de Zeeuw-van Dalfsen, 2019) that are usually difficult to estimate accurately. At Kīlauea, the water table is situated roughly half a kilometer below the surface and experiences minor fluctuations (Johnson et al., 2010; Kauahikaua, 1993). The local gravity change from transient hydrological effects is therefore expected to be minor and not considered here.

Uncertainties in vertical deformation estimates are estimated to be about 2 cm (≈6 μGal), representing the maximum mismatch between the GNSS and InSAR observations. Deviations from the theoretical free-air gradient impose additional uncertainties that are not easily quantified. The local free-air gradient depends significantly on the source of deformation and may be different for, for example, post-glacial rebound (Olsson et al., 2015) compared to volcano deformation involving subsurface fluid redistribution, where the free-air gradient or Bouguer corrected free-air gradient (Vajda et al., 2020, 2021) may be more suitable. Free-body geometry inversions (Camacho et al., 2021) or coupled inversions of surface deformation and gravity (Nikkhoo & Rivalta, 2021) may provide an alternative to recover source parameters; however, mass accumulation without commensurate surface deformation that involves non-elastic behavior, for example, density changes through degassing or the compressibility of gas-rich magma (Rivalta & Segall, 2008), makes joint inversions of gravity and deformation nontrivial. Furthermore, because multiple processes and sources may have been active over the 2009–2015 period, we adopted a classical approach, applying a (theoretical) correction for the observed vertical surface deformation before completing point source gravity inversions.

4.3. Microgravity Changes During 2009–2017 at Kīlauea

4.3.1. Shallow Mass Accumulation Without Commensurate Surface Deformation

Campaign microgravity results indicate that over the course of the 2008–2018 summit eruption, mass accumulated at shallow depth beneath Kīlauea Caldera (Figure 4 and Table 2). The point source solution is the most robust when the microgravity observations are integrated over eight campaigns between 2009 and 2015, indicating mass accumulation on the order of 1.9×10^{11} kg at a depth of roughly 1.3 km below sea level. The source inversion from the April 2017 campaign yielded unrealistic results because of its sparse measurements and low data quality. The recovered depth and position of mass accumulation is slightly below the expected level of the HMMR at approximately 0–1 km below sea level (Bemelmans et al., 2021; Poland et al., 2014). The discrepancy between the expected depth of the HMMR and the recovered center of mass accumulation may be explained by the trade-off in gravity between depth and mass, and the added challenge of recovering accurate depth estimates from surface measurements. Another probable cause is that the observed gravitational effect is a combination of mass accumulation in both the HMMR and SCR, integrated in a single estimate. Furthermore, the recovered depth represents a point source, and the *real* spheroid reservoir boundaries may overlap with geodetic sources presented in the literature (Bemelmans et al., 2021; Jo et al., 2015). Alternatively, geodetic and gravity changes may be sensitive to other distinct parts of the plumbing system.

The relatively continuous subsurface mass accumulation occurred even during periods characterized by subsidence (Figure 4; Poland, Miklius, et al. (2021)). Deformation at Kīlauea during the 2008–2018 eruption began as subsidence between 2009—2010, progressed toward minor uplift inside Kīlauea Caldera during 2011–2012, and turned into significant uplift at the estimated surface position of the SCR following May 2014. The rapid rate of uplift that occurred after May 2014 in the south part of Kīlauea Caldera marked a new phase in the eruption, with increased pressurization eventually leading to a magmatic intrusion in the summit area during May 2015 (Bemelmans et al., 2021; Jo et al., 2015). Even during this period of intense inflation above the SCR, microgravity observations indicate that mass continued to accumulate mainly near the HMMR. This discrepancy may arise from the fact that mass accumulation in the SCR was too distant from the dense network of benchmarks to be fully characterized. Any such deep variations in mass may also be obscured by shallower mass accumulation near the HMMR. In case half of the observed mass accumulates near the HMMR at a reference depth of 500 m b.s.l. and the other half occurs in the SCR at 3,000 m b.s.l. (Poland, Miklius, et al., 2021) the felt gravity change at the surface above the reservoirs would be 280 and 40 μGal respectively. The individual contributions are difficult to estimate because only the integrated amount of gravity change is observed at the surface.

The apparent discrepancy between microgravity observations and surface deformation has been recognized by all previous investigations that compared microgravity campaigns and surface displacements at Kīlauea (Bagnardi et al., 2014; Dzurisin et al., 1980; Johnson et al., 2010). The discrepancy between gravity changes and deformation is also commonly observed worldwide (e.g., Miller et al., 2017; 2018). Assuming a simple Mogi point source (Mogi, 1958) located at the recovered 1.3 km depth b.s.l., with a total volume change of 9.5×10^7 m^3 ($\delta V = \delta M/\rho$), calculated from the recovered 1.9×10^{11} source mass (δM), and an assumed magma density of 2000 kg m^{-3} (ρ). With these parameters, the expected vertical deformation at the surface above the source would exceed 4 m, while the observed vertical deformation (≈20 cm) explains only about 5% of the predicted deformation. This simple estimate suggests that a process is required that accommodates mass increase without corresponding volume increase.

Dzurisin et al. (1980) and Johnson et al. (2010) proposed that the driving process may be the filling of voids below the surface of Kīlauea in a network of interconnected cracks. The existence of such void space is indicated by the difference between the volume of the summit eruptive vent and that of the associated ejecta following its formation in March 2008—the ejecta accounted for only 1% of the volume of the source crater (Houghton et al., 2011). However, part of the material may have been assimilated in the plumbing system and flowed toward the ERZ. Likewise, gravity changes measured during 2018–2019, following the summit collapse and lower ERZ eruption, suggested the presence and filling of voids beneath Kīlauea Caldera (Poland et al., 2019). Complementary to the idea of void space, Bagnardi et al. (2014) offered an alternative explanation that invoked densification of magma in the reservoir through degassing or the compressibility of gas-rich magma (Rivalta & Segall, 2008)—in which the void space is effectively contained within the magma itself.

4.3.2. Lava Lake and Reservoir Density Changes

The gravity response to the summit lava level was greatest at three benchmarks: HOVL-G, HVO41, and 204YY, in order of proximity from the summit vent (HVO41 is illustrated Figure 1 and the benchmarks nearest to the lava lake are HOVL-G and 204YY respectively). Bagnardi et al. (2014) removed the effect of changes in the lava lake on these benchmarks using a geometric model of the conduit before completing point source inversions and found comparable point source estimates to the results presented here. Here, the point source inversions are completed excluding the observed changes at these benchmarks. Excluding these benchmarks reduces the biasing of the point source inversion results toward the eruptive vent, in case such a geometric forward model fails to capture the observed disruptive vent changes between campaigns. As an added benefit, the recovered point sources (Table 2) can be used to isolate the gravity effect of the lava lake at these benchmarks (Figure 8, bottom). Comparison of results between the forward model used by Bagnardi et al. (2014) and that from Figure 8 (bottom) shows that the gravity effect of the lava lake appears similar. The isolated effect between March 2011—November 2012 shows a similar increase for benchmarks HVO41 and 205YY (100 μGal) as calculated by the forward model of Bagnardi et al. (2014). The isolated effect on benchmark HOVL-G however, is about 50–100 μGal higher, presumably because it is closer to the source and more sensitive to inaccuracies.

The period stretching from March 2011 to June 2012 spans the most variation in the lava lake level (Figure 8). The nearest benchmarks show an increase in gravity that is small compared to the much steeper increase in gravity between June 2012 and November 2012, despite a smaller rise in the level of the lava lake. This difference may imply that the density of the lava lake was higher in 2012 compared to 2011, producing larger gravity change for smaller lava lake level change. In the period between November 2012 and September 2015, the level of the lava lake remained relatively stable at an elevated level, except during the May 2015 summit intrusion (Bemelmans et al., 2021). The decrease in gravity at the benchmarks nearest to the summit eruptive vent between November 2012 and November 2013 may be a result of the rim collapse that occurred in January 2013 and the loss of 21,000 m^3 of material (Patrick, Swanson, & Orr, 2019), effectively replacing solid rock with air. After 2014, InSAR data (Figure 4—row 1) show consistent inflation without commensurate changes to the level of the lava lake. In the case that the lava lake is in magmastatic equilibrium with the deeper magmatic system, an increase in subsurface pressure that leads to surface deformation would also probably lead to an increased lava level inside the summit vent. Such rise in the lava lake level is not observed, and the stability of the lava lake level over this period may instead be explained by an increase in magmastatic pressure inside the summit vent. The density increase may occur in the reservoir or at the top of the conduit and be recycled into the deeper reservoir after degassing. Such magmastatic increase in pressure as a result of higher magma density (ρgh) would counteract the increased deeper pressurization in order to keep the lava level stable, while the surrounding region continued to inflate. Alternatively, Patrick, Swanson, and Orr (2019) suggest that after 2014 the lava lake level does not change proportionally with deformation because the pressurization occurs within the SCR instead of the HMMR (Figure 4). This hypothesis requires that the SCR and HMMR are not strongly connected. With a direct connection between the reservoirs, deep pressurization would be felt throughout the entire plumbing system, including the HMMR, and be expressed in the lava lake level. The suggested hypothesis for the stability of the lava lake during this period thus appears contingent on the assumed configuration of the plumbing system. After September 2015, the level of the lava lake rose steadily, but changes in microgravity for this period were only available for benchmark HVO41. At that time, it may be that the density of the magma was reaching its bubble-free limit—forcing pressure increases coming from the deeper magmatic system to be accommodated by rising lava lake level once more.

A quantitative analysis of microgravity results from the summit vent benchmarks is challenging because of the long interval between campaigns, and the fact that major disruptive events modified the vent geometry. Continuous gravity observations from the rim of the summit eruptive vent support that lava lake density did increase over time, from roughly 950 ± 300 kg m^{-3} in 2011 (Carbone et al., 2013), climbing toward 1,000–1,500 kg m^{-3} between 2011 and 2015 (Poland & Carbone, 2016), and up to 1,700 kg m^{-3} by the time of the 2018 lower ERZ eruption (Poland, Carbone, & Patrick, 2021).

An increase in magma density in the lava lake inside the summit eruptive vent may indicate, when considering the observation of subsurface mass accumulation without commensurate surface deformation, that densification also took place throughout the subsurface magma reservoirs. Significant variations in magma density in the shallow reservoir have also been detected through seismic techniques (Crozier & Karlstrom, 2021), and significant degassing took place based on the increased rate of SO_2 emissions coming from the summit (Elias et al., 2018;

Sutton & Elias, 2014) after the opening of the vent. Similarly, the frequency of gas pistoning events—sudden changes in lava level driven by gas accumulation and release in the upper part of the lava lake—decreased from 2010—2015 (Patrick et al., 2016), indicating that less gas-rich, denser magma was becoming more prevalent in the reservoir. Multiple independent observations, including the campaign microgravity results presented here, thus support the hypothesis of densification of magma within the magmatic system.

4.3.3. Implications of Density Changes for Magma Supply Rates

The magma supply rate at Kīlauea has a fundamental impact on the character (e.g., rate, volume, and duration) of its eruptions (Dvorak & Dzurisin, 1993; Poland et al., 2012; Swanson, 1972). Variations in the supply rate of Kīlauea's magmatic system have previously been estimated directly from outflow volumes, or through proxy measurements such as ground deformation or gas emissions. These estimates indicated an above average supply rate between 2003—2006 before the summit eruption began, and a potential lull in magma supply rate between 2011 and 2012 (Anderson & Poland, 2016), likely returning to pre-eruption levels by 2016 (Dzurisin & Poland, 2019). The magma-supply models are often based on mass-balance equations that assume incompressible magma and thus do not account for the potential influence of magma density changes inside the magma storage reservoirs. One consequence of this approach is that the inferred decrease in supply during 2011–2012 may potentially be overestimated because (some portion of) the supply was accommodated by the compression and densification of gas-rich magma. The presented estimate of the amount of subsurface mass accumulated beneath Kīlauea Caldera from microgravity campaigns may provide additional constraints that might improve magma supply rate estimates.

4.3.4. Potential Effects of Densification on Eruption Behavior

Another implication of magma densification is that a column of high density magma may increase pressure in other parts of the magmatic system. One possible example is the summit intrusion in May 2015, which was preceded by a rise in lava level overflowing the summit vent in Halema‘uma‘u crater. The sudden rise in lava lake level was followed by a drop of similar magnitude, as an intrusion was emplaced below the southern part of Kīlauea Caldera (Bemelmans et al., 2021; Patrick, Swanson, & Orr, 2019), providing an alternative outlet for the excess pressure. A similar mechanism may have contributed to expediting the lower ERZ eruption in 2018. Increased (magmastatic) pressure from Kīlauea's summit area was probably felt throughout the volcano's magmatic system, as indicated by inflation that was especially strong along the ERZ and at the summit in the weeks prior to the 2018 lower ERZ outbreak (Patrick et al., 2020; Poland et al., 2022). The increased magmastatic pressure of the magma filling Kilauea's summit reservoirs may thus have contributed to the breaking of a barrier toward the ERZ on April 30, which allowed the summit reservoir and lower-elevation plumbing system of dense accumulated magma to feed the LERZ eruption, as is expected from microstructural constraints of the erupted magma (Wieser et al., 2020). Microgravity results can provide no additional information on the configuration of the plumbing system below Kīlauea Caldera. Whether the ERZ is sourced by the HMMR (Wang et al., 2021) or the SCR (Wieser et al., 2020) is unknown.

5. Conclusion

Nine microgravity campaigns were completed at Kīlauea between 2009—2017. The data were reduced using a weighted least-squares approach (Hwang et al., 2002), which proved especially effective in short double-loop circuits. Derived microgravity changes over time illustrate that subsurface mass on the order of 1.9×10^{11} kg accumulated beneath Kīlauea Caldera during 2009–2015. The mass increase was identified at an average depth of 1.3 km below sea level, slightly below the expected position of the shallow Halema‘uma‘u reservoir from alternative geodetic observations. The accumulation of mass had probably been occurring since 1975 (Bagnardi et al., 2014; Johnson et al., 2010) and continued until the 2018 eruptive outbreak in the lower ERZ. The accumulation of subsurface mass beneath Kīlauea Caldera was not commensurate with the observed surface deformation. This discrepancy may be caused by densification of magma inside the Halema‘uma‘u reservoir through a combination of degassing through the summit eruptive vent and the densification and compression of gas-rich magma (Rivalta & Segall, 2008)—a conclusion that might impact apparent changes in magma supply over time and that argues for the inclusion of microgravity data in modeling of magma supply rates. When magma compressibility and densification continue to counteract increasing pressure from the deeper plumbing system, excess pressure may be relieved through alternative means. Such transfer of pressure accommodation mechanisms in Kīlauea's summit area might explain activity like the 2015 summit intrusion and may have even expedited the devastating lower ERZ outbreak in 2018.

Data Availability Statement

Microgravity campaign data are published by the USGS (Flinders et al., 2022). InSAR data were obtained from the German Aerospace Center (DLR) and the Italian Space Agency (ASI) via the Hawai'i Supersite. Ocean loading parameters were derived from the free ocean loading service, accessible at http://holt.oso.chalmers.se/loading/. Seismometer data was downloaded from the USGS Hawaiian Volcano Observatory (HVO) (1956). Digital elevation model data were downloaded from the USGS (2015). Analysis code was written in Python 3.8.2 (Van Rossum & Drake, 2009) using SciPy (Virtanen et al., 2020) and NumPy (Harris et al., 2020). Figures were made with Matplotlib (Hunter, 2007), version 3.2.1 (Caswell et al., 2020) and a pre-release version of PyGMT (Uieda et al., 2021) using Generic Mapping Tools version 6 (Wessel et al., 2019a, 2019b). A web application that implements the applied weighted least-squares approach is available online at: https://jollyfant.github.io/g-campaign-solve-js/ (Koymans, 2022).

Acknowledgments

The authors would like to thank the JGR Solid Earth (associate) editor for their comments. Reviewers Taiyi Wang, Craig Miller, and Kyle Anderson are greatly thanked for their thorough reviews of the manuscript. The authors also express our gratitude to the USGS staff for their suggestions. Your comments have led to the serious improvement of many aspects of this paper. Maurizio Battaglia is thanked for discussion and suggestions on how to apply ocean loading corrections and Duncan Agnew is thanked for his advice using HARDISP. We are grateful to the staff of the Hawaiian Volcano Observatory for their support of gravity measurements at Kīlauea. All of the data described in this report were collected within Hawai'i Volcanoes National Park, and we are grateful for the collaboration and support of numerous Hawai'i Volcanoes National Park staff over the years in facilitating our gravity monitoring and research efforts. Any use of trade, firm, or product names is for descriptive purposes only and does not imply endorsement by the U.S. Government. This work was supported by the NEWTON-g project, which has received funding from the EC's Horizon 2020 programme, under the FETOPEN-2016/2017 call (Grant Agreement No 801221).

References

Agnew, D. (2010). HARDISP. IERS conventions (2010). *IERS Tech. Note*, *36*, 99–122.

Anderson, K. R., Johanson, I. A., Patrick, M. R., Gu, M., Segall, P., Poland, M. P., et al. (2019). Magma reservoir failure and the onset of caldera collapse at Kīlauea Volcano in 2018. *Science*, *366*(6470), eaaz1822. https://doi.org/10.1126/science.aaz1822

Anderson, K. R., N, A., Foster, J. H., & Frazer, N. (2020). Implications of deflation-inflation event models on Kīlauea Volcano, Hawai'i. *Journal of Volcanology and Geothermal Research*, *397*, 106832. https://doi.org/10.1016/j.jvolgeores.2020.106832

Anderson, K. R., & Poland, M. P. (2016). Bayesian estimation of magma supply, storage, and eruption rates using a multiphysical volcano model: Kīlauea Volcano, 2000 – 2012. *Earth and Planetary Science Letters*, *447*, 161–171. https://doi.org/10.1016/j.epsl.2016.04.029

Anderson, K. R., Poland, M. P., Johnson, J. H., & Miklius, A. (2015). Episodic deflation-inflation events at Kīlauea Volcano and implications for the shallow magma system. In *Hawaiian volcanoes* (pp. 229–250). John Wiley & Sons, Inc. https://doi.org/10.1002/9781118872079.ch11

Bagnardi, M., Poland, M. P., Carbone, D., Baker, S., Battaglia, M., & Amelung, F. (2014). Gravity changes and deformation at Kīlauea Volcano, Hawai'i, associated with summit eruptive activity, 2009 – 2012. *Journal of Geophysical Research: Solid Earth*, *119*(9), 7288–7305. https://doi.org/10.1002/2014jb011506

Battaglia, M., Lisowski, M., Dzurisin, D., Poland, M. P., Schilling, S., Diefenbach, A., & Wynn, J. (2018). Mass addition at mount st. helens, Washington, inferred from repeated gravity surveys. *Journal of Geophysical Research: Solid Earth*, *123*(2), 1856–1874. https://doi.org/10.1002/2017jb014990

Battaglia, M., Patre, A. C.-D., & Flinders, A. F. (2022). gTOOLS, an open-source MATLAB program for processing high precision, relative gravity data for time-lapse gravity monitoring. *Computers & Geosciences*, *160*, 105028. https://doi.org/10.1016/j.cageo.2021.105028

Battaglia, M., Poland, M. P., & Kauahikaua, J. (2012). GTOOLS: An interactive computer program to process gravity data for high-resolution applications. *AGU fall meeting abstracts*, *2012*, GP43B–1143.

Beilin, J. (2006). *Apport de la gravimétrie absolue à la réalisation de la composante gravimétrique du Réseau Géodésique Français*. Institut Géographique National.

Bemelmans, M. J., de Zeeuw-van Dalfsen, E., Poland, M. P., & Johanson, I. A. (2021). Insight into the May 2015 summit inflation event at Kīlauea Volcano, Hawai'i. *Journal of Volcanology and Geothermal Research*, *415*, 107250. https://doi.org/10.1016/j.jvolgeores.2021.107250

Bos, M., & Scherneck, H. (2014). Onsala space observatory. Retrieved from http://holt.oso.chalmers.se/loading/

Camacho, A. G., Vajda, P., Miller, C. A., & Fernández, J. (2021). A free-geometry geodynamic modelling of surface gravity changes using growth-dg software. *Scientific Reports*, *11*(1), 1–17. https://doi.org/10.1038/s41598-021-02769-z

Carbone, D., Antoni-Micollier, L., Hammond, G., de Zeeuw-van Dalfsen, E., Rivalta, E., Bonadonna, C., et al. (2020). The Newton-g gravity imager: Toward new paradigms for terrain gravimetry. *Frontiers of Earth Science*, *452*. https://doi.org/10.3389/feart.2020.573396

Carbone, D., Cannavò, F., Greco, F., Reineman, R., & Warburton, R. J. (2019). The benefits of using a network of superconducting gravimeters to monitor and study active volcanoes. *Journal of Geophysical Research: Solid Earth*, *124*(4), 4035–4050. https://doi.org/10.1029/2018jb017204

Carbone, D., & Greco, F. (2007). Review of microgravity observations at Mt. Etna: A powerful tool to monitor and study active volcanoes. *Pure and Applied Geophysics*, *164*(4), 769–790. https://doi.org/10.1007/s00024-007-0194-7

Carbone, D., & Poland, M. P. (2012). Gravity fluctuations induced by magma convection at Kīlauea Volcano, Hawai'i. *Geology*, *40*(9), 803–806. https://doi.org/10.1130/g33060.1

Carbone, D., Poland, M. P., Diament, M., & Greco, F. (2017). The added value of time-variable microgravimetry to the understanding of how volcanoes work. *Earth-Science Reviews*, *169*, 146–179. https://doi.org/10.1016/j.earscirev.2017.04.014

Carbone, D., Poland, M. P., Patrick, M. R., & Orr, T. R. (2013). Continuous gravity measurements reveal a low-density lava lake at Kīlauea Volcano, Hawai'i. *Earth and Planetary Science Letters*, *376*, 178–185. https://doi.org/10.1016/j.epsl.2013.06.024

Caswell, T. A., Droettboom, M., Lee, A., Hunter, J., Firing, E., Stansby, D., et al. (2020). matplotlib/matplotlib: Rel: V3.2.1 [Software]. Zenodo. https://doi.org/10.5281/zenodo.3714460

Cattin, R., Mazzotti, S., & Baratin, L.-M. (2015). GravProcess: An easy-to-use MATLAB software to process campaign gravity data and evaluate the associated uncertainties. *Computers & Geosciences*, *81*, 20–27. https://doi.org/10.1016/j.cageo.2015.04.005

Crozier, J., & Karlstrom, L. (2021). Wavelet-based characterization of very-long-period seismicity reveals temporal evolution of shallow magma system over the 2008 – 2018 eruption of Kīlauea Volcano. *Journal of Geophysical Research: Solid Earth*, *126*(6), e2020JB020837. https://doi.org/10.1029/2020jb020837

Dehant, V., Defraigne, P., & Wahr, J. (1999). Tides for a convective Earth. *Journal of Geophysical Research*, *104*(B1), 1035–1058. https://doi.org/10.1029/1998jb900051

Dvorak, J. J., & Dzurisin, D. (1993). Variations in magma supply rate at Kīlauea Volcano, Hawai'i. *Journal of Geophysical Research*, *98*(B12), 22255–22268. https://doi.org/10.1029/93jb02765

Dzurisin, D., Anderson Kyle, R. L. A., Eaton, G. P., Koyanagi, R. Y., Lipman, P. W., Lockwood, J. P., et al. (1980). Geophysical observations of Kīlauea Volcano, Hawai'i, 2. Constraints on the magma supply during November 1975 – September 1977. *Journal of Volcanology and Geothermal Research*, *7*(3–4), 241–269. https://doi.org/10.1016/0377-0273(80)90032-3

Dzurisin, D., & Poland, M. P. (2019). Magma supply to Kīlauea volcano, Hawai'i, from inception to now: Historical perspective, current state of knowledge, and future challenges. In *Field volcanology: A tribute to the distinguished career of don Swanson*. Geological Society of America. https://doi.org/10.1130/2018.2538(12)

Egbert, G. D., & Erofeeva, S. Y. (2002). Efficient inverse modeling of barotropic ocean tides. *Journal of Atmospheric and Oceanic Technology*, *19*(2), 183–204. https://doi.org/10.1175/1520-0426(2002)019<0183:eimobo>2.0.co;2

Elias, T., Kern, C., Horton, K. A., Sutton, A. J., & Garbeil, H. (2018). Measuring SO_2 emission rates at Kīlauea Volcano, Hawai'i, using an array of upward-looking UV spectrometers, 2014 – 2017. *Frontiers of Earth Science*, *6*, 214. https://doi.org/10.3389/feart.2018.00214

Flinders, A. F., Poland, M. P., Conway, S., Bagnardi, M., Battaglia, M., Brantley, S., et al. (2022). Data of the Hawaiian Volcano Observatory Kīlauea campaign gravity network (KCGN) (2009 – 2017) [Dataset]. U.S. Geological Survey data release. https://doi.org/10.5066/P9INL9SG

Fowler, C. M. R., Fowler, C. M. R., & Fowler, M. (1990). *The solid Earth: An introduction to global geophysics*. Cambridge University Press.

Giniaux, J. M., Hooper, A. J., & Bagnardi, M. (2017). New methods for assessing and reducing uncertainty in microgravity studies. In *AGU fall meeting abstracts* (Vol. 2017, p. G54A–06).

Harris, C. R., Millman, K. J., van der Walt, S. J., Gommers, R., Virtanen, P., Cournapeau, D., et al. (2020). Array programming with NumPy [Software]. Nature, *585*(7825), 357–362. https://doi.org/10.1038/s41586-020-2649-2

Hector, B., & Hinderer, J. (2016). pyGrav, a Python-based program for handling and processing relative gravity data. *Computers & Geosciences*, *91*, 90–97. https://doi.org/10.1016/j.cageo.2016.03.010

Houghton, B., Swanson, D., Carey, R., Rausch, J., & Sutton, A. (2011). Pigeonholing pyroclasts: Insights from the 19 March 2008 explosive eruption of Kīlauea Volcano. *Geology*, *39*(3), 263–266. https://doi.org/10.1130/g31509.1

Hunter, J. D. (2007). Matplotlib: A 2D graphics environment. *Computing in Science & Engineering*, *9*(3), 90–95. https://doi.org/10.1109/MCSE.2007.55

Hwang, C., Wang, C.-G., & Lee, L.-H. (2002). Adjustment of relative gravity measurements using weighted and datum-free constraints. *Computers & Geosciences*, *28*(9), 1005–1015. https://doi.org/10.1016/s0098-3004(02)00005-5

Jachens, R. C., & Eaton, G. P. (1980). Geophysical observations of Kīlauea Volcano, Hawai'i, 1. Temporal gravity variations related to the 29 November, 1975, m = 7.2 earthquake and associated summit collapse. *Journal of Volcanology and Geothermal Research*, *7*(3–4), 225–240. https://doi.org/10.1016/0377-0273(80)90031-1

Jo, M.-J., Jung, H.-S., & Won, J.-S. (2015). Detecting the source location of recent summit inflation via three-dimensional InSAR observation of Kīlauea Volcano. *Remote Sensing*, *7*(11), 14386–14402. https://doi.org/10.3390/rs71114386

Johnson, D. J. (1992). Dynamics of magma storage in the summit reservoir of Kīlauea Volcano, Hawai'i. *Journal of Geophysical Research*, *97*(B2), 1807–1820. https://doi.org/10.1029/91jb02839

Johnson, D. J., Eggers, A. A., Bagnardi, M., Battaglia, M., Poland, M. P., & Miklius, A. (2010). Shallow magma accumulation at Kīlauea Volcano, Hawai'i, revealed by microgravity surveys. *Geology*, *38*(12), 1139–1142. https://doi.org/10.1130/g31323.1

Kauahikaua, J. (1993). Geophysical characteristics of the hydrothermal systems of Kīlauea Volcano. *Hawai'i. Geothermics*, *22*(4), 271–299. https://doi.org/10.1016/0375-6505(93)90004-7

Kauahikaua, J., & Miklius, A. (2003). Long-term trends in microgravity at Kīlauea's summit during the Pu'u Ō'ō-Kūpaianaha eruption. *U. S. Geological Survey Professional Paper*, *1676*(1676), 165.

Kennedy, J. R. (2021). GSadjust [Software]. U.S. Geological Survey. https://doi.org/10.5066/P9YEIOU8

Koymans, M. R. (2022). Web application for microgravity campaign analysis [Software]. Zenodo. https://doi.org/10.5281/zenodo.6466389

Longman, I. (1959). Formulas for computing the tidal accelerations due to the Moon and the Sun. *Journal of Geophysical Research*, *64*(12), 2351–2355. https://doi.org/10.1029/jz064i012p02351

Lundgren, P., Poland, M. P., Miklius, A., Orr, T., Yun, S.-H., Fielding, E., et al. (2013). Evolution of dike opening during the March 2011 Kamoamoa fissure eruption, Kīlauea Volcano, Hawai'i. *Journal of Geophysical Research: Solid Earth*, *118*(3), 897–914. https://doi.org/10.1002/jgrb.50108

McCubbine, J., Tontini, F. C., Stagpoole, V., Smith, E., & O'Brien, G. (2018). Gsolve, a Python computer program with a graphical user interface to transform relative gravity survey measurements to absolute gravity values and gravity anomalies. *SoftwareX*, *7*, 129–137. https://doi.org/10.1016/j.softx.2018.04.003

Middlemiss, R., Samarelli, A., Paul, D., Hough, J., Rowan, S., & Hammond, G. (2016). Measurement of the Earth tides with a MEMS gravimeter. *Nature*, *531*(7596), 614–617. https://doi.org/10.1038/nature17397

Miller, C., Le Mével, H., Currenti, G., Williams-Jones, G., & Tikoff, B. (2017). Microgravity changes at the Laguna del Maule volcanic field: Magma-induced stress changes facilitate mass addition. *Journal of Geophysical Research: Solid Earth*, *122*(4), 3179–3196. https://doi.org/10.1002/2017jb014048

Miller, C. A., Currenti, G., Hamling, I., & Williams-Jones, G. (2018). Mass transfer processes in a post eruption hydrothermal system: Parameterisation of microgravity changes at Te Maari craters, New Zealand. *Journal of Volcanology and Geothermal Research*, *357*, 39–55. https://doi.org/10.1016/j.jvolgeores.2018.04.005

Mogi, K. (1958). Relations between the eruptions of various volcanoes and the deformations of the ground surfaces around them. *Earthq Res Inst*, *36*, 99–134.

Murray, A. S., & Tracey, R. M. (2001). Best practice in gravity surveying. *Geoscience Australia*, *3*(5).

Neal, C. A., Brantley, S., Antolik, L., Babb, J., Burgess, M., Calles, K., et al. (2019). The 2018 rift eruption and summit collapse of Kīlauea Volcano. *Science*, *363*(6425), 367–374. https://doi.org/10.1126/science.aav7046

Nikkhoo, M., & Rivalta, E. (2021). Analytical solutions for gravity changes caused by triaxial volumetric sources. *Earth and Space Science Open Archive ESSOAr*. https://doi.org/10.1002/essoar.10507706.1

Olsson, P.-A., Milne, G., Scherneck, H.-G., & Ågren, J. (2015). The relation between gravity rate of change and vertical displacement in previously glaciated areas. *Journal of Geodynamics*, *83*, 76–84. https://doi.org/10.1016/j.jog.2014.09.011

Orr, T. R., Poland, M. P., Patrick, M. R., Thelen, W. A., Sutton, A. J., Elias, T., et al. (2015). Kīlauea 5 – 9 March 2011 Kamoamoa fissure eruption and its relation to 30+ years of activity from Pu'u 'Ō'ō. *Hawaiian Volcanoes: From Source to Surface*, *208*, 393.

Patrick, M. R., Houghton, B. F., Anderson, K. R., Poland, M. P., Montgomery-Brown, E., Johanson, I., et al. (2020). The cascading origin of the 2018 Kīlauea eruption and implications for future forecasting. *Nature Communications*, *11*(1), 5646. https://doi.org/10.1038/s41467-020-19190-1

Patrick, M. R., Orr, T., Anderson, K. R., & Swanson, D. (2019a). Eruptions in sync: Improved constraints on Kīlauea Volcano's hydraulic connection. *Earth and Planetary Science Letters*, *507*, 50–61. https://doi.org/10.1016/j.epsl.2018.11.030

Patrick, M. R., Orr, T., Sutton, A., Lev, E., Thelen, W., & Fee, D. (2016). Shallowly driven fluctuations in lava lake outgassing (gas pistoning), Kīlauea Volcano. *Earth and Planetary Science Letters*, *433*, 326–338. https://doi.org/10.1016/j.epsl.2015.10.052

Patrick, M. R., Swanson, D., & Orr, T. (2019b). A review of controls on lava lake level: Insights from Halema'uma'u crater, Kīlauea volcano. *Bulletin of Volcanology*, *81*(3), 13. https://doi.org/10.1007/s00445-019-1268-y

Poland, M. P. (2014). Time-averaged discharge rate of subaerial lava at Kīlauea Volcano, Hawai'i, measured from TanDEM-X interferometry: Implications for magma supply and storage during 2011 – 2013. *Journal of Geophysical Research: Solid Earth*, *119*(7), 5464–5481. https://doi.org/10.1002/2014jb011132

Poland, M. P., & Carbone, D. (2016). Insights into shallow magmatic processes at Kīlauea Volcano, Hawai'i, from a multiyear continuous gravity time series. *Journal of Geophysical Research: Solid Earth*, *121*(7), 5477–5492. https://doi.org/10.1002/2016jb013057

Poland, M. P., & Carbone, D. (2018). Continuous gravity and tilt reveal anomalous pressure and density changes associated with gas pistoning within the summit lava lake of Kīlauea Volcano, Hawai'i. *Geophysical Research Letters*, *45*(5), 2319–2327. https://doi.org/10.1002/2017gl076936

Poland, M. P., Carbone, D., & Patrick, M. R. (2021a). Onset and evolution of Kīlauea's 2018 flank eruption and summit collapse from continuous gravity. *Earth and Planetary Science Letters*, *567*, 117003. https://doi.org/10.1016/j.epsl.2021.117003

Poland, M. P., & de Zeeuw-van Dalfsen, E. (2019). Assessing seasonal changes in microgravity at Yellowstone Caldera. *Journal of Geophysical Research: Solid Earth*, *124*(4), 4174–4188. https://doi.org/10.1029/2018jb017061

Poland, M. P., de Zeeuw-van Dalfsen, E., Bagnardi, M., & Johanson, I. A. (2019). Post-collapse gravity increase at the summit of Kīlauea Volcano, Hawai'i. *Geophysical Research Letters*, *46*(24), 14430–14439. https://doi.org/10.1029/2019gl084901

Poland, M. P., Hurwitz, S., Kauahikaua, J. P., Montgomery-Brown, E. K., Anderson, K. R., Johanson, I. A., et al. (2022). Rainfall an unlikely factor in Kīlauea's 2018 rift eruption. *Nature*, *602*(7895), E7–E10. https://doi.org/10.1038/s41586-021-04163-1

Poland, M. P., Miklius, A., Jeff Sutton, A., & Thornber, C. R. (2012). A mantle-driven surge in magma supply to Kīlauea Volcano during 2003 – 2007. *Nature Geoscience*, *5*(4), 295–300. https://doi.org/10.1038/ngeo1426

Poland, M. P., Miklius, A., Johanson, I. A., & Anderson, K. R. (2021b). *A decade of geodetic change at Kīlauea's summit – observations, interpretations, and unanswered questions from studies of the 2008 – 2018 Halema'uma'u eruption*. US Geological Survey Professional Paper. chap G. https://doi.org/10.3133/pp1867g

Poland, M. P., Miklius, A., & Montgomery-Brown, E. K. (2014). Magma supply, storage, and transport at shield-stage Hawaiian volcanoes (pp. 179–234). https://doi.org/10.3133/pp18015

Powell, M. J. (1964). An efficient method for finding the minimum of a function of several variables without calculating derivatives. *The Computer Journal*, *7*(2), 155–162. https://doi.org/10.1093/comjnl/7.2.155

Rau, G. C. (2018). Hydrogeoscience/Pygtide: Pygtide V0.2 [Software]. Zenodo. Retrieved from https://zenodo.org/record/1346664

Reilly, W. (1970). Adjustment of gravity meter observations. *New Zealand Journal of Geology and Geophysics*, *13*(3), 697–702. https://doi.org/10.1080/00288306.1970.10431341

Reudink, R., Klees, R., Francis, O., Kusche, J., Schlesinger, R., Shabanloui, A., et al. (2014). High tilt susceptibility of the Scintrex CG-5 relative gravimeters. *Journal of Geodesy*, *88*(6), 617–622. https://doi.org/10.1007/s00190-014-0705-0

Rivalta, E., & Segall, P. (2008). Magma compressibility and the missing source for some dike intrusions. *Geophysical Research Letters*, *35*(4), L04306. https://doi.org/10.1029/2007gl032521

Rymer, H. (1994). Microgravity change as a precursor to volcanic activity. *Journal of Volcanology and Geothermal Research*, *61*(3–4), 311–328. https://doi.org/10.1016/0377-0273(94)90011-6

Scintrex Limited, C. (2012). CG-5 Scintrex autograv system operation manual.

Sutton, A., & Elias, T. (2014). *One hundred volatile years of volcanic gas studies at the Hawaiian Volcano Observatory*. US Geological Survey Professional Paper. https://doi.org/10.3133/pp18017

Swanson, D. A. (1972). Magma supply rate at Kīlauea Volcano, 1952 – 1971. *Science*, *175*(4018), 169–170. https://doi.org/10.1126/science.175.4018.169

Uieda, L., Tian, D., Leong, W., Toney, L., Schlitzer, W., Grund, M., et al. (2021). PyGMT: A Python interface for the generic mapping tools [Software]. PyGMT.

USGS. (2015). Kīlauea digital elevation model (10m) [Dataset]. SOEST. Retrieved from http://www.soest.hawaii.edu/coasts/data/hawaii/dem.html

USGS Hawaiian Volcano Observatory (HVO). (1956). Hawaiian Volcano Observatory network [Dataset]. International Federation of Digital Seismograph Networks. https://doi.org/10.7914/SN/HV

Vajda, P., Foroughi, I., Vaníček, P., Kingdon, R., Santos, M., Sheng, M., & Goli, M. (2020). Topographic gravimetric effects in Earth sciences: Review of origin, significance and implications. *Earth-Science Reviews*, *211*, 103428. https://doi.org/10.1016/j.earscirev.2020.103428

Vajda, P., Zahorec, P., Miller, C. A., Le Mével, H., Papčo, J., & Camacho, A. G. (2021). Novel treatment of the deformation–induced topographic effect for interpretation of spatiotemporal gravity changes: Laguna del maule (Chile). *Journal of Volcanology and Geothermal Research*, *414*, 107230. https://doi.org/10.1016/j.jvolgeores.2021.107230

Van Camp, M., de Viron, O., Watlet, A., Meurers, B., Francis, O., & Caudron, C. (2017). Geophysics from terrestrial time-variable gravity measurements. *Reviews of Geophysics*, *55*(4), 938–992. https://doi.org/10.1002/2017rg000566

Van Camp, M., & Vauterin, P. (2005). TSoft: Graphical and interactive software for the analysis of time series and Earth tides. *Computers & Geosciences*, *31*(5), 631–640. https://doi.org/10.1016/j.cageo.2004.11.015

Van Rossum, G., & Drake, F. L. (2009). *Python 3 reference manual*. CreateSpace.

Virtanen, P., Gommers, R., Oliphant, T. E., Haberland, M., Reddy, T., Cournapeau, D., et al. (2020). SciPy 1.0: Fundamental algorithms for scientific computing in Python [Software]. Nature Methods, *17*(3), 261–272. https://doi.org/10.1038/s41592-019-0686-2

Wang, T., Zheng, Y., Pulvirenti, F., & Segall, P. (2021). Post-2018 caldera collapse re-inflation uniquely constrains Kīlauea's magmatic system. *Journal of Geophysical Research: Solid Earth*, *126*(6). https://doi.org/10.1029/2021jb021803

Wenzel, H.-G. (1996). The nanogal software: Earth tide data processing package ETERNA 3.30. *Bull. Inf. Marées Terrestres*, *124*, 9425–9439.

Werner, C., Wegmüller, U., Strozzi, T., & Wiesmann, A. (2000). Gamma SAR and interferometric processing software. *Proceedings of the ERS-ENVISAT Symposium* (Vol. 1620, p. 1620).

Wessel, P., Luis, J., Uieda, L., Scharroo, R., Wobbe, F., Smith, W. H., & Tian, D. (2019a). The generic mapping tools version 6 [Software]. Geochemistry, Geophysics, Geosystems, *20*(11), 5556–5564. https://doi.org/10.1029/2019gc008515

Wessel, P., Luis, J. F., Uieda, L., Scharroo, R., Wobbe, F., Smith, W. H. F., & Tian, D. (2019b). The generic mapping tools version 6 [Software]. Zenodo. https://doi.org/10.5281/zenodo.3407866 Funded by US National Science Foundation grants OCE-1558403 and EAR-1829371.

Wieser, P. E., Edmonds, M., Maclennan, J., & Wheeler, J. (2020). Microstructural constraints on magmatic mushes under kīlauea volcano, Hawaii. *Nature Communications*, *11*(1), 1–14. https://doi.org/10.1038/s41467-019-13635-y

Wijaya, D. D., Muhamad, N. A., Prijatna, K., Sadarviana, V., Sarsito, D. A., Pahlevi, A., & Putra, W. (2019). pyGABEUR-ITB: A free software for adjustment of relative gravimeter data. *Geomatika*, *25*(2), 95–102. https://doi.org/10.24895/jig.2019.25-2.991

Yun, S., Segall, P., & Zebker, H. (2006). Constraints on magma chamber geometry at sierra negra volcano, galápagos islands, based on InSAR observations. *Journal of Volcanology and Geothermal Research*, *150*(1–3), 232–243. https://doi.org/10.1016/j.jvolgeores.2005.07.009